AN UPDATED PROCEDURE FOR TARE AND INTERFERENCE WIND TUNNEL TESTING OF STRUT-MOUNTED MODELS

A Thesis

by

DOUGLAS MICHAEL KUTZ

Submitted to the Office of Graduate and Professional Studies of
Texas A&M University
in partial fulfillment of the requirements for the degree of

MASTER OF SCIENCE

Chair of Committee,	Edward White
Co-Chair of Committee,	Thomas Strganac
Committee Member,	Stefan Hurlebaus
Head of Department,	Rodney Bowersox

May 2014

Major Subject: Aerospace Engineering

ABSTRACT

Despite advances in modern computing and simulation, wind tunnel testing remains the most trusted method for determining aerodynamic vehicle behavior. Corrections are applied to accurately obtain results representative of free-air performance due to the presence of wind tunnel walls. The standard correction procedure adjusts for the presence of these boundaries using approximations based on linear potential flow theory. Separately, tare and interference removal involves the linear subtraction of mounting strut effects, accomplished using mirrored mounting systems. Uncertainty in wind tunnel data is quantified throughout each step in the data analysis procedure. Additionally, an updated procedure for the analysis and correction of wind tunnel data for strut mounted models is recommended.

ACKNOWLEDGEMENTS

I would first like to thank my advisor, Dr. White. His teaching, reassurance, and guidance throughout the past few years are responsible for the success of this project. Also, thank you to my committee members, Dr. Strganac and Dr. Hurlebaus, for their assistance in this work. I would like to extend a special thank you to the staff of the Texas A&M Oran W. Nicks Low Speed Wind Tunnel for their endless patience and support. Thank you to my colleagues Alex Herring and Tanner Black for their continued support while conducting this research, even through the difficult times. Lastly, thank you to my family, who have provided the endless encouragement that made this work a reality.

TABLE OF CONTENTS

LIST OF FIGURES

LIST OF TABLES

TABLE Page

1. INTRODUCTION

1.1 Background and Objective

Wind tunnel testing remains an important tool for understanding the behavior of bodies immersed in fluid flow. Models are tested to assess aerodynamic performance and vehicle stability. Benjamin Robins's whirling arm apparatus was employed as the only testing device until the late 19th century when Frank H. Wenham operated the first wind tunnel, moving air past the test article rather than the converse [1].

Testing is necessary because the Navier-Stokes equations that govern fluid motion do not have a general analytic solution and can only be solved analytically for special cases or solved numerically using intensive numerical simulation. The field of computational fluid dynamics (CFD) is an important one, as wind tunnel testing is an expensive undertaking. Aerodynamicists can execute a large portion of the design and optimization phases without requiring a wind tunnel. Despite a surge in computing power, wind tunnels remain necessary because some phenomena still cannot be reliably predicted using CFD. As such, an important function of wind tunnels is the validation of CFD results. In all cases, it is desirable for the resulting data to be representative of free-flight vehicle behavior.

The aerodynamic response measured during a wind tunnel test necessarily differs from free-flight behavior due to the existence of the test section boundaries. Data are made more representative of free-flight by accounting for wall effects and effects of the model mounting hardware. A well-established technique for achieving this is outlined by Barlow, Rae and Pope [2]. A series of linear wall and blockage "corrections" was developed in the middle 20th century. Barlow et al. also outline a testing procedure for strut-mounted tests that allows for the removal of effects arising from

a mounting strut. This is accomplished by testing a model configuration while both upright and inverted. A mirror-image mounting system is also used for this procedure, a setup which reveals any flow angularity present in the test section. Data from equivalent runs are subtracted from each other, resulting in support-free data. Much like the wall correction techniques, the procedure for the removal of mounting hardware effects is based on a simple linear model. Despite a substantial increase in computing power since the advent of these techniques, the same approximations used to simplify the calculations remain in place, potentially causing avoidable errors in the resulting data. Surprisingly however, the uncertainty associated with the wall-correction methodology has yet to be quantified.

This thesis aims to quantify the error introduced into the final "free-air" data due to the use of approximation and the assumption of linearity. With upflow present in the test section, a direct subtraction of upright and inverted data in practice may introduce errors due to the fact that the upright and inverted configurations are not precisely equivalent (see Figure 1.1). Errors will be quantified by comparing the data resulting from the standard correction procedure outlined by Barlow et al. to that resulting from a modified approach. One modification to the approach is the removal of all simplifications presumably arising from lack of computing power, including small angle approximations such as $\sin\alpha \approx \alpha$. Additionally, an interpolation step will be added so that the removal of support effects will be computed for equivalent configurations. Data uncertainty will be monitored and propagated throughout each step of the data analysis procedure in order to make direct comparisons between approaches. Finally, recommendations will be made as to whether the rigorous computations are indeed necessary and whether the interpolation step is needed for removal of support effects.

The following sections describe the facility used to execute large-scale wind tunnel

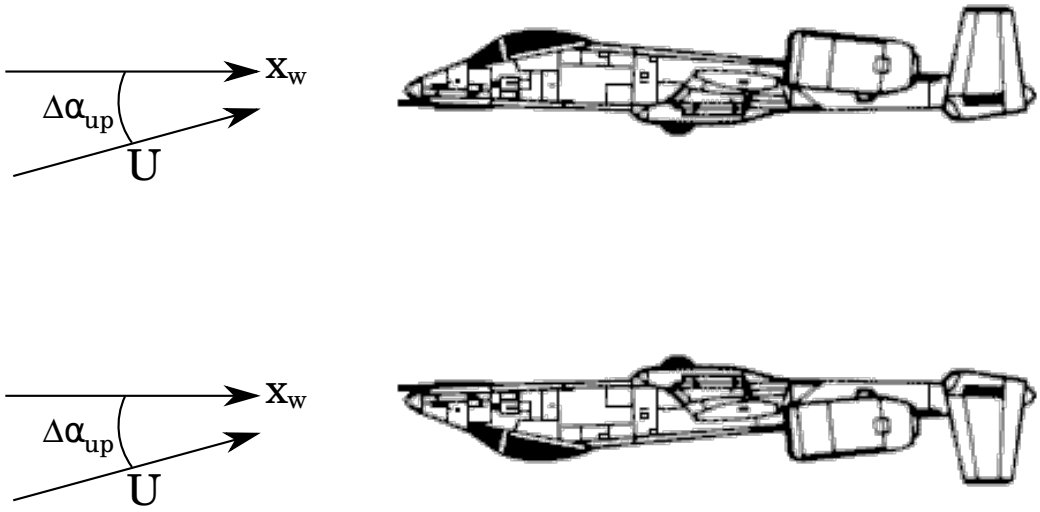

Figure 1.1: Angle of attack discrepancy between upright ($\phi = 0°$) and inverted ($\phi = 180°$) orientations.

testing of a strut-mounted models, followed by an explanation of the standard testing and data reduction processes. An example of one of these tests will be discussed in detail, followed by a review of the standard testing technique, where recommendations will be made about the validity and accuracy of the current approach.

1.2 Tare and Interference Testing Principles & Example

The tare and interference testing approach is a standard method for execution of a wind tunnel test where aerodynamic forces and moments on a strut-mounted model are measured using an external balance. This method makes balance data more representative of free-air flight behavior by estimating and removing the effects associated with the presence of the support strut. At the crux of the tare and interference strategy is the assumption that both the tare (the effect of the strut's presence alone on balance measurements) and the interference effects (the effect of the strut on the flow around the test article plus the converse) can be linearly subtracted from the measured data. In order to estimate tare and interference (T&I) effects, the test article must feature an image strut system which allows mounting in upright ($\phi = 0°$) and inverted ($\phi = 180°$) orientations while matching the amount of support strut exposure underneath the model (ventral surface). Following the recommendations of Barlow, Rae and Pope [2], execution of a tare and interference sequence requires three sets of runs: inverted with and without an image system and upright without the image system. The setup for these three configurations is shown in Figure 1.2.

Tare and interference affects all aerodynamic loads. For specificity, consider just the drag force. The measured drag in the upright configuration with a strut penetrating the ventral surface is $D_{\text{meas,up}} = D_{\text{true}} + T_L + I_L$, the sum of the true drag, the lower-strut tare T_L and the interference drag I_L on the vehicle due to the lower strut

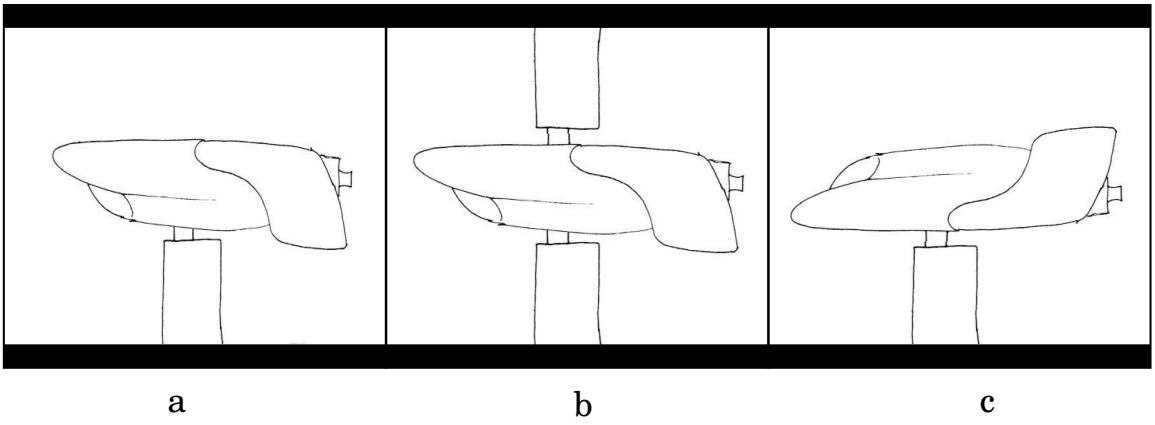

Figure 1.2: T&I setup: (a) inverted without image, $\phi = 180°$, (b) inverted with image, $\phi = 180°$, (c) upright without image, $\phi = 0°$

and fairing (which may be positive or negative). The task is to remove the $T_L + I_L$ contributions to the measured drag to reveal the "true" drag that would presumably affect the vehicle in free flight. It is not necessary to separate the contributions of T_L and I_L so they are lumped as TI_L.

To find TI_L, two inverted runs are performed, with and without an image strut penetrating the ventral surface. The image strut in this configuration is identical to the "lower" strut that connects the model to the balance in the upright configuration. Thus, it retains the subscript L in this orientation. The strut connecting the model to the external balance is referred to as the "upper" strut (subscript U) in the inverted orientation. The image (lower) strut is metric and small clearance between it and the image strut fairing (needed for symmetry) avoids an unwanted load path from the model. The measured drag in the two inverted orientations are

$$D_{\text{meas,inv/out}} = D_{\text{true}} + TI_U$$

$$D_{\text{meas,inv/in}} = D_{\text{true}} + TI_U + TI_L$$

where the subscripts inv/out and inv/in indicate "inverted, image strut out" and "inverted, image strut in" respectively. Subtracting $D_{\text{meas,inv/out}}$ from $D_{\text{meas,inv/in}}$ yields an estimate of TI_L. This can subsequently be subtracted from the measured drag in the upright orientation $D_{\text{meas,up}}$ to give an estimate of the true drag because $D_{\text{meas,up}} = D_{\text{true}} + TI_L$. Figures 1.3 and 1.4 show the drag and lift TI_L as a function of α for an inverted ($\phi = 180°$) model configuration. TI_L remains fairly constant with α but departs sharply near stalled regions. Additionally, the T&I effect is virtually nonexistent in the lift force, but affects drag by as much as 60% near $C_{D,\text{min}}$. The lift component of TI_L is slightly positive near $\alpha = 0°$ because of the flow angularity induced by the lower strut. Without the image system, the induced upflow angle due to the lower strut causes the model to experience a greater lift force than the equivalent configuration with the image system.

Figures 1.5 and 1.6 show the effect of linearly subtracting TI_L from upright, gravity-tare-removed data. Because separation is a nonlinear phenomenon, a point-by-point subtraction such as this may behave unpredictably – especially in unstable regions – due to the discrepancy in angle of attack discussed above. The TI_L curve shows a discontinuity at $\alpha = -12°$, presenting another potential source of error associated with the direct subtraction method.

The T&I calculations are all performed in the wind-oriented coordinate system at the balance moment reference center. To account for small variations in the point-by-point dynamic pressure, the forces and moments are non-dimensionalized and given in coefficient form. Forces are divided by $q_{\text{act}}S$ and moments by $q_{\text{act}}Sb$ or $q_{\text{act}}S\,\bar{c}$, where q_{act} is the dynamic pressure and S, b, and $\bar{c}$ are respectively the wing planform area, span and mean aerodynamic chord (MAC).

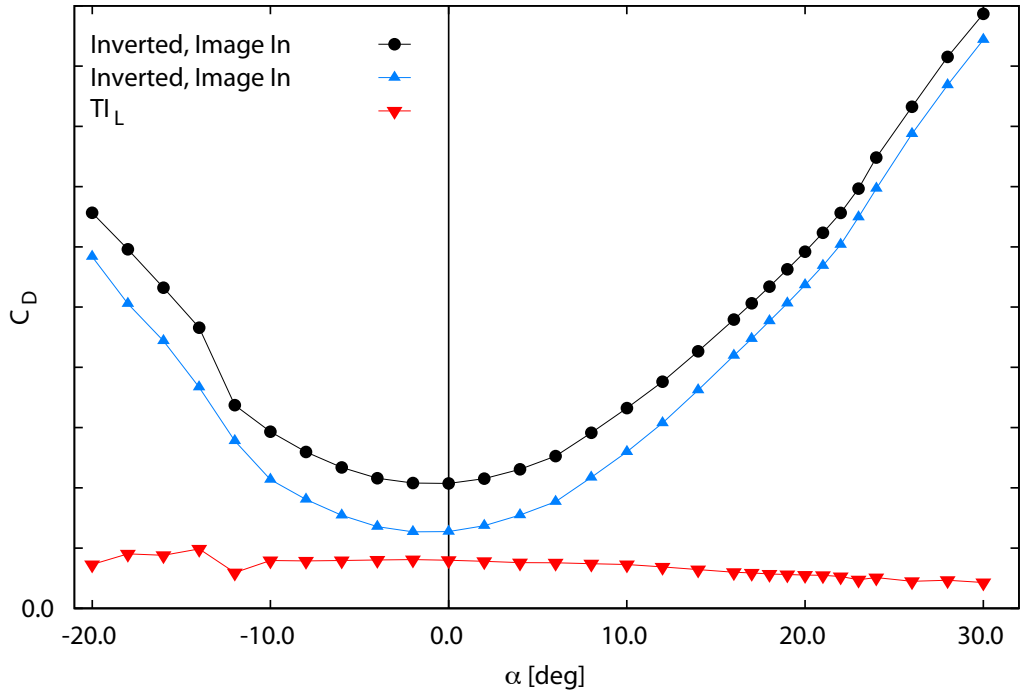

Figure 1.3: Pitch sweep: inverted T&I drag data

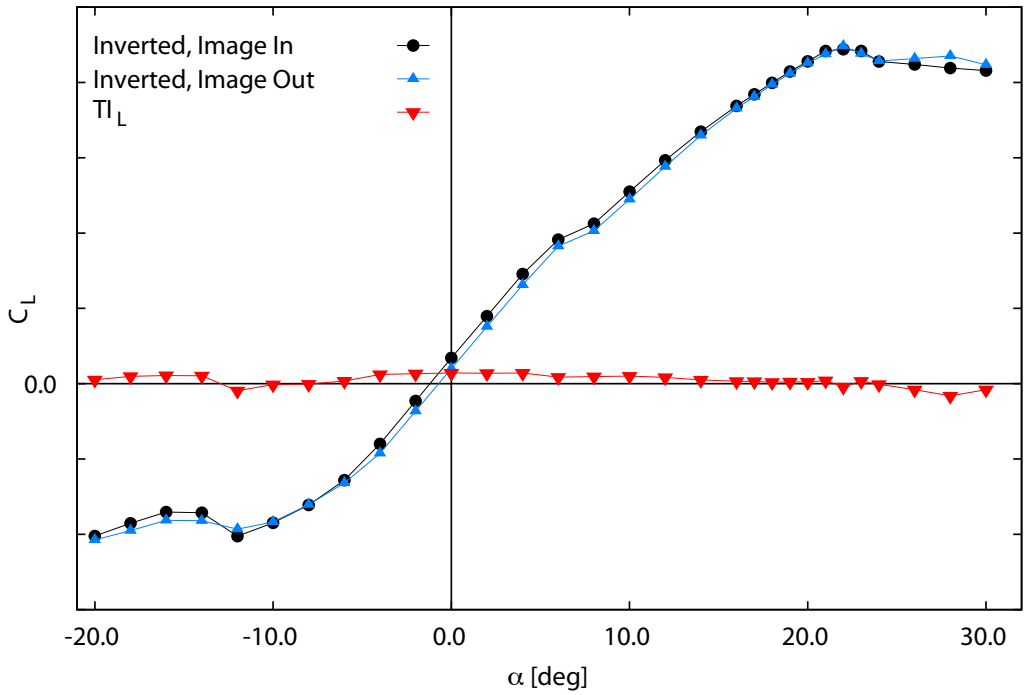

Figure 1.4: Pitch sweep: inverted T&I lift data

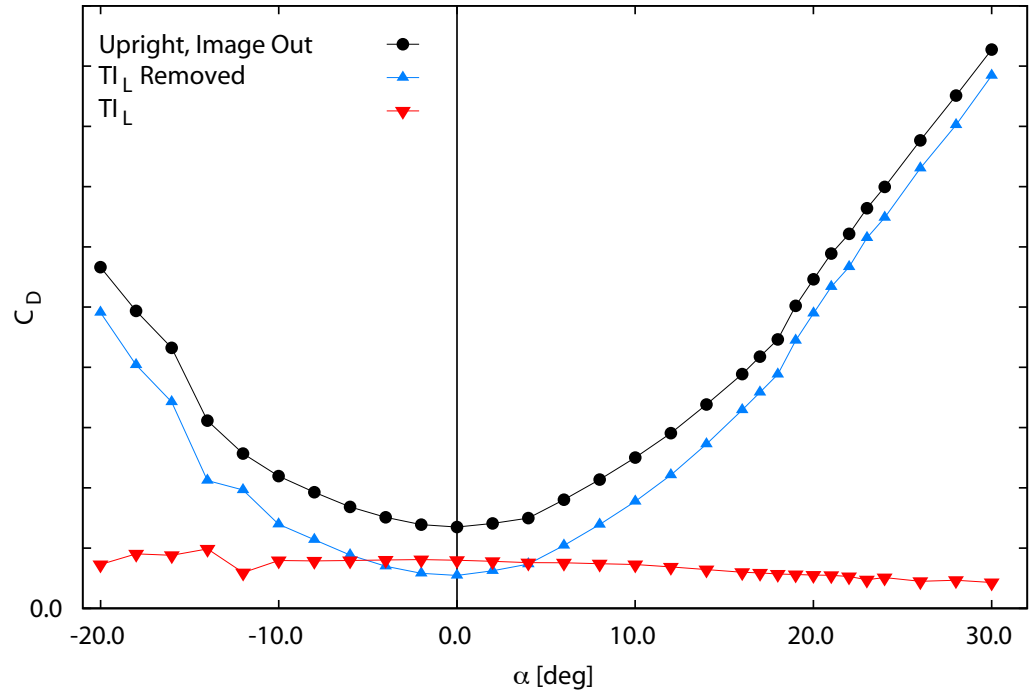

Figure 1.5: Pitch sweep: T&I-removed drag data

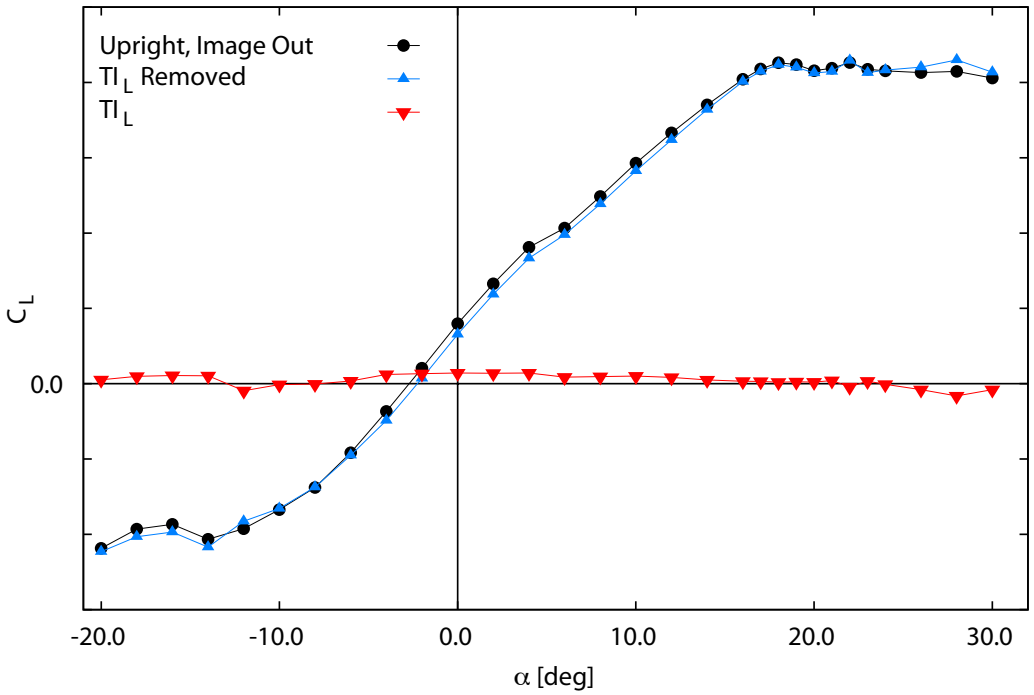

Figure 1.6: Pitch sweep: T&I-removed lift data

1.3 Wind Tunnel Boundary Correction Principles

Strut effects are subtracted from data using the technique described in Section 1.2. However, the wind tunnel walls are boundaries that do not exist around the full-scale flight vehicle. The boundaries become streamlines of the flow in order to enforce the no-penetration boundary condition at the walls. The effects of each of the relevant flow phenomena caused by the existence of a wing in flow are contained within the tunnel boundaries using the method of images outlined by Glauert [3]. These phenomena are modelled by linearly superposing infinite sets of mirrored flow singularities – sources and vortices – derived from linear potential flow theory.

Because the behavior of the streamlines flowing past the test model is largely governed by the circulation Γ generated by the wing, the wing itself is modelled as a distribution of vortices. A horseshoe vortex originating at the wing's quarter-chord location remains consistent with Helmholtz's second theorem that a vortex filament can neither begin nor end in a fluid [4]. A simplified illustration of the horseshoe vortex distribution is shown in Figure 1.7. Image vortices model the presence of boundaries by ensuring that only the tangential velocity component exists at the walls. Figure 1.8 shows the direction of the induced velocity for the existing bound vortex V_i and that of the top mirrored vortex $V_{i,m}$. Examining the top half of the system, the bound vortex and image vortex are equidistant from a given boundary, meaning their effect on the flow at the boundary is equivalent. The no-penetration condition is enforced since the vertical components of the induced velocity vectors sum to zero. Enforcing the tunnel boundary conditions modifies the flow field in the vicinity of the model. The modified flow field causes a change in the aerodynamic response of the model, necessitating a set of data corrections to make measurements more representative of free flight.

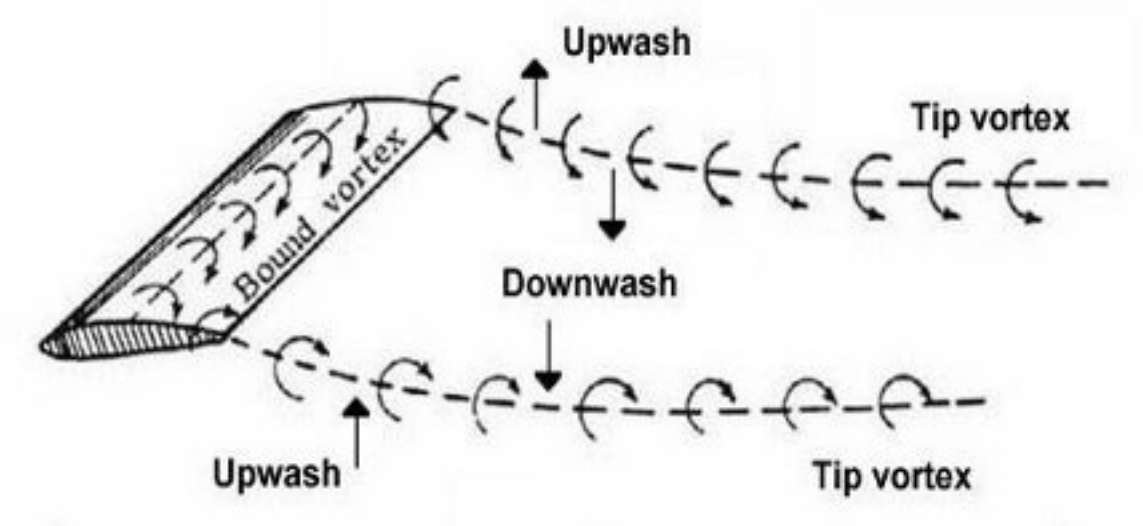

Figure 1.7: Horseshoe vortex comprised of bound vortex at quarter-chord and trailing tip vortices

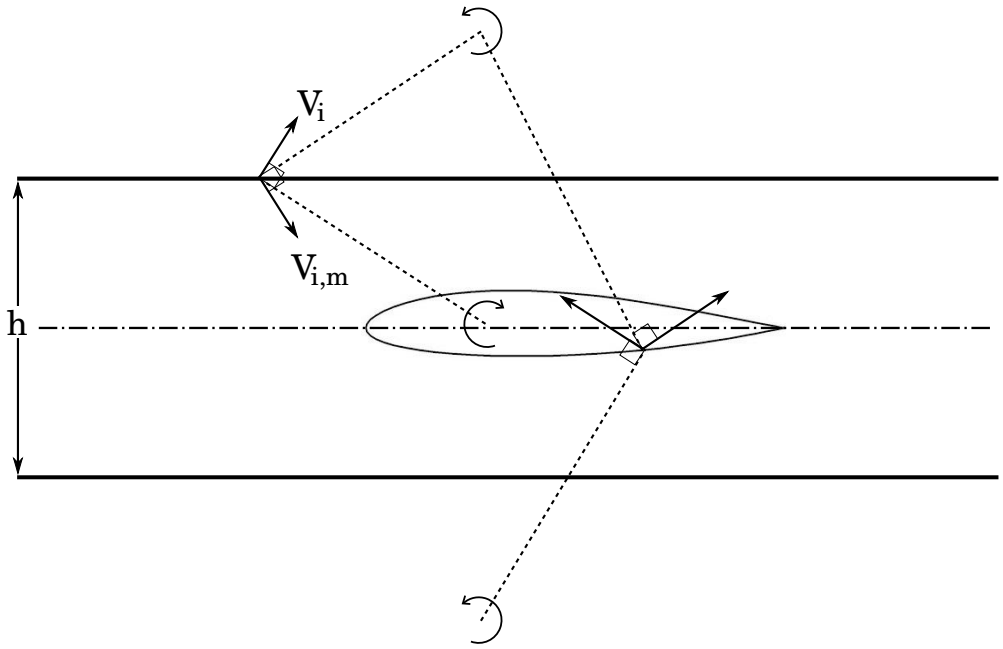

Figure 1.8: First image system vortex pair for bound vortex filament

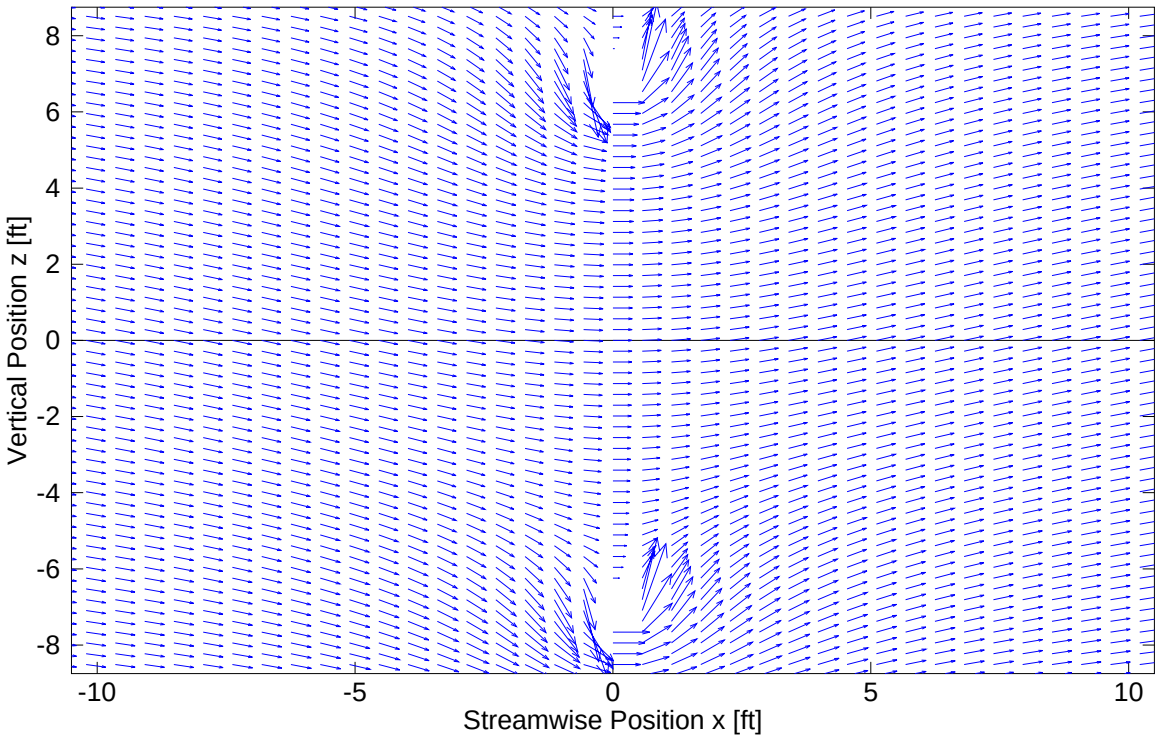

Figure 1.9: Flow field resulting from bound vortex image systems.

The vertical image systems for the bound vortex filament effectively constrict the resulting streamlines such that the body appears more cambered and at greater angle of attack (see Figure 1.9). The induced angle of attack due to the vertical image systems (bounding the vortices along the wing's span) is referred to as the streamline curvature correction.

The wingtip trailing vortices are bounded using similar logic (see Figure 1.10). In free flight, tip vortices generate downwash which induces an angle of attack at the tail. The presence of the wind tunnel walls alters the downwash that would be seen by the tail in free flight (see Figure 1.11). The foremost result is an alteration in pitching moment. Additionally, the altered downwash causes too large a minimum drag and too small a lift-curve slope. The induced angle of attack due to the horizontal image

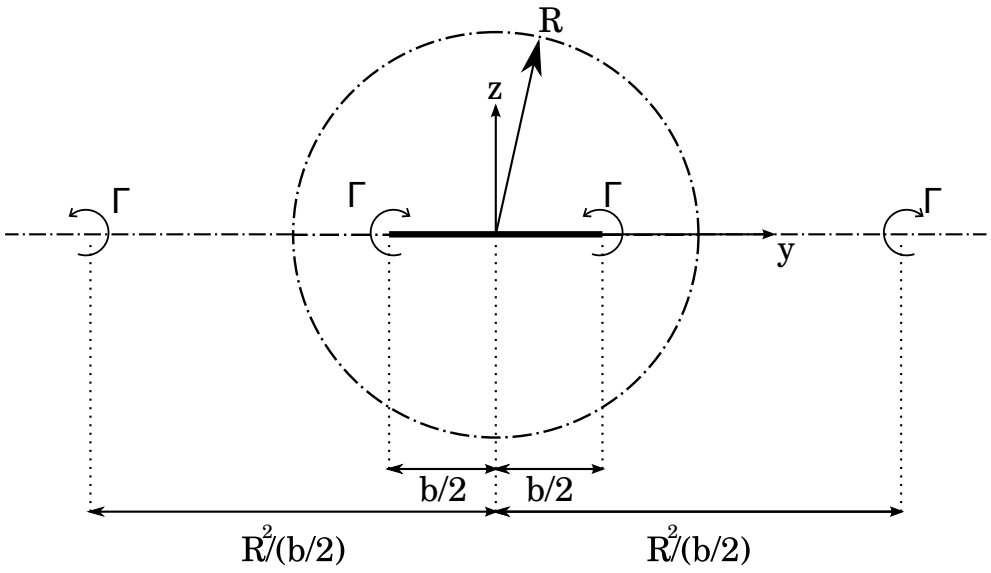

Figure 1.10: First image system vortex pair for trailing tip vortices

system (bounding the trailing tip vortices) is referred to as the normal downwash correction.

The streamline curvature and normal downwash corrections both affect the angularity of the flow field around the model. Another source of flow angularity is aerodynamic balance misalignment. This accounts for a discrepancy between the upstream flow direction and the balance's drag direction. The misalignment is estimated by executing one upright-model pitch sweep with the image strut installed. Comparing the lift curves for the upright and inverted model configuration, both with the image system installed, reveals a discrepancy at equivalent upright and inverted angles of attack. Because the configurations are nominally symmetric, differences in the lift curves of the two configurations arise due to upflow in the test section. The shift in the lift curve is $2\Delta\alpha_{\text{up}}$ where $\Delta\alpha_{\text{up}}$ is the upflow angle and is assumed to be

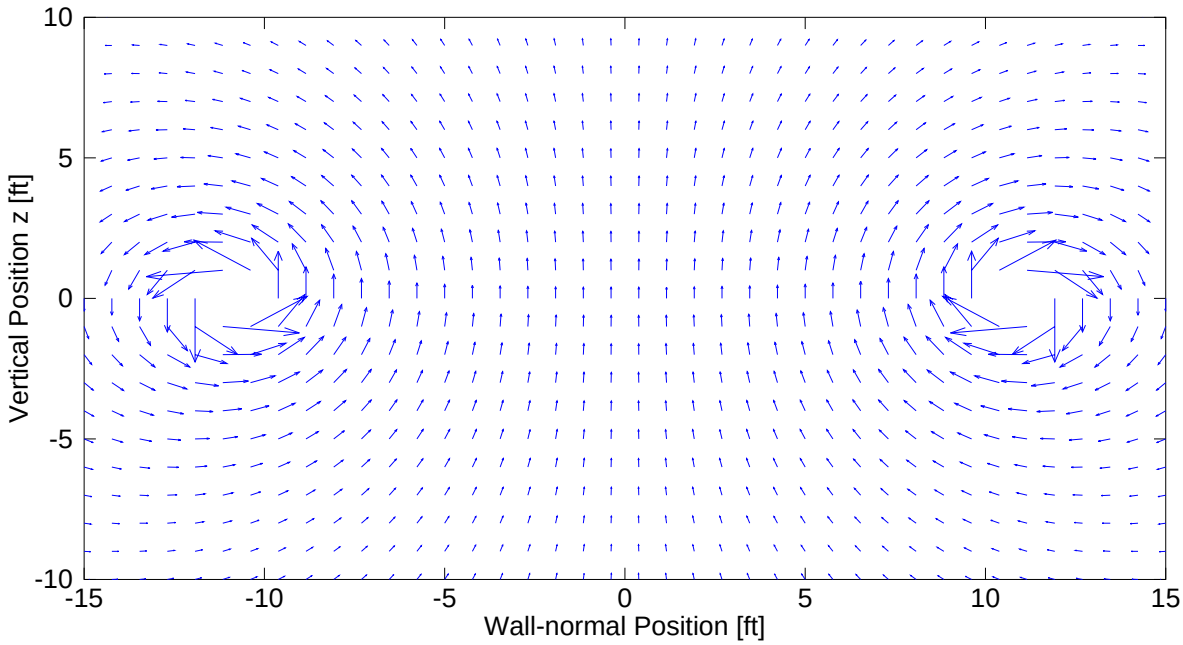

Figure 1.11: Flow field resulting from trailing tip vortices and image systems.

constant spatially (x_w, y_w, z_w) and insensitive to model attitude (α, β, ϕ). Figure 1.12 shows the discrepancy in the upright and inverted configuration lift curves due to upflow.

In addition to flow angularity, the presence of the model effects a change in the effective test section cross sectional area which causes a change in the effective dynamic pressure. Two corrections are applied. The solid blockage correction depends only on model and wind tunnel geometry. Constant mass flux requires $A_1V_1 = A_2V_2$. A_1 and A_2 respectively represent the test section cross sectional area with and without blockage, and V_1 and V_2 are the corresponding flow velocities. The presence of the model causes $A_2 > A_1$ and hence $V_1 > V_2$. In practice, the solid blockage velocity increment is proportional to the ratio of model volume to test section volume, but includes other terms derived from empirical data. The wake blockage correction is derived by placing a line source at the trailing edge of the wing to represent the

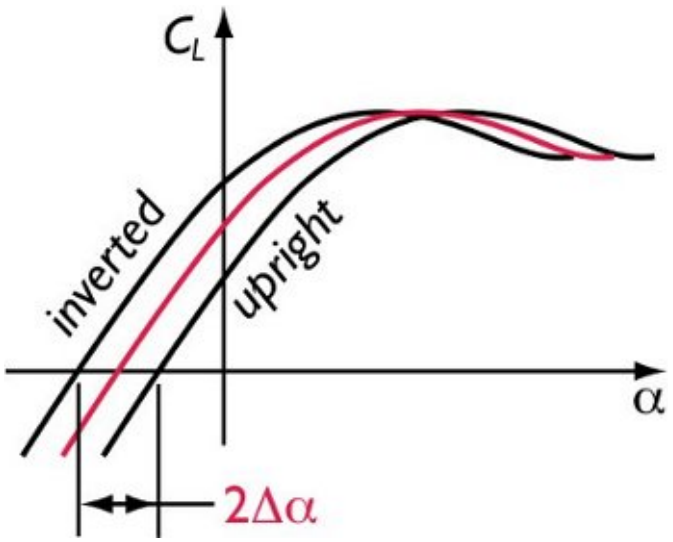

Figure 1.12: Lift discrepancy (inverted vs. upright) due to upflow

accelerated fluid in the region outside the decelerated wake. The flow stagnates upstream of the source to form a Rankine half-body as the model of the wake. To preserve continuity, a line sink of equal strength is placed downstream at $x \to +\infty$. Again, an infinite system of sources and sinks is then distributed above and below the trailing edge source. The result is an increment in flow velocity due to the wake blockage in the test section.

2. LOW SPEED WIND TUNNEL FACILITY DETAILS

Section 1 discussed the principles and motivation behind wind tunnel testing. The goal of the following section is to introduce the reader to a wind tunnel facility used for a variety of industries. The testing and data analysis techniques discussed previously are primarily employed for vehicles tested by the aerospace industry. The facility details and operational notes described below will also help to motivate discussions in later sections.

2.1 Oran W. Nicks Low Speed Wind Tunnel Overview

The Oran W. Nicks Low Speed Wind Tunnel (LSWT) at Texas A&M is a large-scale closed circuit wind tunnel (Appendix A) facility. It was erected as an open-circuit tunnel in 1948, and has since undergone various renovations and modifications which have improved upon the accuracy of experimental measurements and have added to the overall capability of the facility. Among these improvements are the conversion of the LSWT to a closed-circuit tunnel in 1958 and the addition of a 3000 HP motor with variable-frequency drive system in 2013 to couple with the existing variable-pitch propeller. In combination, these modifications help to improve the overall efficiency of the wind tunnel and allow for a greater range of free stream conditions while maintaining high-quality flow. For a more in-depth history of the Oran W. Nicks LSWT, see Hidore [5].

The LSWT circuit length at the centerline is 398 feet. The tunnel cross section is circular from the power section at the exit of the diffuser around to the entrance of the contraction section. The maximum diameter of 30 feet occurs in the settling chamber. Turning vanes are located at each of four 90° turns in the circuit. A single screen, located at the settling chamber entrance, and a double screen upstream of

the contraction section provide a uniform inflow and reduce turbulence.

The test section is 14 feet long, 7 feet high and 10 feet wide with one-foot corner chamfers. Its cross sectional area is 68 ft^2. Three inch vertical venting slots in the side walls at the test section exit maintain test section static pressure near atmospheric pressure. The test section walls diverge about 1 inch in 12 feet to account for boundary layer growth and eliminate streamwise buoyancy. A 7-ft-diameter floor turntable rotates with the external balance system. Access to the test section is through a removable ceiling and an overhead crane. Fluorescent lights are positioned in the corner fillets. The test-section side walls are large plate glass windows. A 30-ft-long contraction section acts as a transition from the circular to the rectangular cross section. The contraction ratio is 10.4. A 46-ft-long diffuser downstream of the test section returns the flow to a circular cross section. The horizontal and vertical expansion angles of the diffuser are 1.43° and 3.38°, respectively. The tunnel fan is a variable-pitch 12.5-ft-diameter, four-blade Curtiss Electric propeller. It is driven by a 3000 hp variable-speed Teco-Westinghouse motor. Blade tips are inset into the tunnel wall to minimize tip interference effects. Test section dynamic pressures between zero and 100 psf (200 mph) can be obtained by adjusting the blade pitch and speed.

The external balance is a six-component, pyramidal electromechanical system located on the first floor of the facility, below the test section. It resolves aerodynamic forces and moments in a wind-oriented coordinate system with its origin the geometric center of the test section. Force, moment and attitude measurements are transmitted to the data acquisition system control via optical encoders. The balance turntable yaw range is $-120°$ to $+190°$. Lift force can be measured from -1000 lb to $+3000$ lb; drag and side force can be measured from ± 1000 lb. Forces are accurate to the greater of 0.2 lb or 0.2% of the applied load. Pitching and rolling moments

can be measured to ±2000 ft·lb; yaw can be measured to ±1000 ft·lb. Moments are accurate to the greater of 0.2 ft·lb or 0.2% of the applied moment. A variety of support systems are available for mounting models to the external balance. Typical models employ one, two or three vertical struts or sting supports. The facility has a selection of such mounting systems suitable for accommodating models.

Electronic pressure instrumentation are available for up to 300 simultaneous measurements. Signal conditioning for strain-gage balances and instruments are available. The test section is outfitted with a three-axis traversing mechanism for hotwire anemometers or pressure probes. This equipment allows the positioning of instrumentation with repeatable accuracy of 0.01 inches.

2.2 Tunnel Operation

Flow speed is controlled using the calculated dynamic pressure of the airflow at the center of the test section. Two static pressure rings, consisting of four ports each, are used to measure the average static pressure drop across the length of the settling chamber. This difference, denoted q_{set}, is used to calibrate the actual dynamic pressure q_{act} in the center of the empty test section. A calibration curve is created and used to calculate q_{act} from q_{set} when the calibration Pitot tube is not installed in the test section. From Hidore, $q_{\text{act}} = 1.042 q_{\text{set}} \pm 0.02$ psf. While the tunnel is in operation, q_{set} is directly measured, and control logic ensures that q_{act} (calculated as part of the control) remains within 0.2% of the prescribed dynamic pressure. This approach provides the test section dynamic pressure that would be measured upstream of any model influence.

The temperature inside the tunnel is measured with a thermocouple that is located on the wall at the beginning of the test section. The barometric pressure is recorded in the balance room, beneath the test section. These measurements are

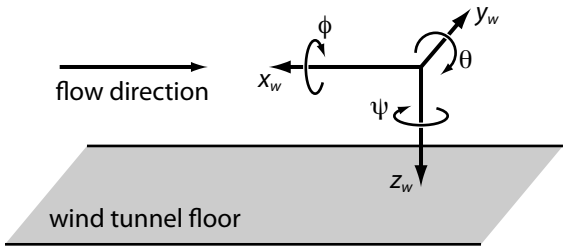

Figure 2.1: Wind-oriented coordinate system

used to calculate tunnel flow speed for the current tunnel conditions. The total and static pressure in the tunnel are also measured during a test using a Pitot tube located on the back ($+y_w$) wall.

2.3 Coordinate System Definitions and Transformations

Various coordinate systems are used during testing following the convention described by Barlow et al. In the wind-oriented coordinate system (shown in Figure 2.1), x_w points upwind, z_w is aligned with the gravity vector and y_w maintains the right-handed system. Rotations about the wind-fixed x_w, y_w and z_w axes are ϕ, θ and ψ, respectively. These angles are used to specify vehicle/model attitude during tests. When the model is upright ($\phi = 0°$), the aerodynamic angles are $\alpha = \theta$ and $\beta = -\psi$. When the model is inverted ($\phi = 180°$), $\alpha = -\theta$ and $\beta = \psi$. The body-oriented coordinate system rotates with the vehicle such that the x_b axis points forward through the nose, y_b points out through the right side of the fuselage and z_b points out (down) through the ventral surface of the fuselage. When the body is upright and at $\theta = \psi = 0°$, the wind axes and body axes are aligned.

The external balance gives forces and moments in the wind oriented coordinate

system, defined as:

$$\begin{aligned} D &= -F_{x_w} \quad S = +F_{y_w} \quad L = -F_{z_w} \\ RM &= +M_{x_w} \quad PM = +M_{y_w} \quad YM = +M_{z_w} \end{aligned}$$

where L, D and S are lift, drag and side force and PM, RM and YM are pitch, roll and yaw moments, respectively. The reference center for the moments measured by the external balance is 42 inches above the wind tunnel floor along the turntable rotation axis, i.e., the geometric reference center of the test section. Typically, an aerodynamic vehicle is mounted with its pitch axis along the test section centerline, 42 inches above the floor. However, the pitch axis may be located some distance fore or aft of the balance moment center (BMC). Furthermore, the model's aerodynamic moment reference center (MRC) may be located at some other location. The transformation from BMC to MRC for a non-rolled model ($\phi = 0°$) is given by:

$$\begin{aligned} x_{\text{MRC}} &= -[dx_{\text{pivot}} + dx_b \cos\theta - dz_b \sin\theta] \cos\psi \\ y_{\text{MRC}} &= -[dx_{\text{pivot}} + dx_b \cos\theta - dz_b \sin\theta] \sin\psi \\ z_{\text{MRC}} &= \quad dx_b \sin\theta + dz_b \cos\theta \end{aligned} \tag{2.1}$$

In Equations 2.1, dx_{pivot} is the horizontal distance (in the x_w direction) between the BMC and pivot point location, and dx_b and dz_b are respectively the horizontal and vertical distances between the pivot point and model MRC. Transferring moments from the BMC to the MRC is then accomplished using:

$$\begin{aligned} RM_{\text{MRC}} &= RM_{\text{BMC}} - z_{\text{MRC}} S - y_{\text{MRC}} L \\ PM_{\text{MRC}} &= PM_{\text{BMC}} - z_{\text{MRC}} D + x_{\text{MRC}} L \\ YM_{\text{MRC}} &= YM_{\text{BMC}} + x_{\text{MRC}} S + y_{\text{MRC}} D \end{aligned} \tag{2.2}$$

In the body axis system, the forces and moments are

$$A = -F_{x_b} \qquad Y = +F_{y_b} \qquad N = -F_{z_b}$$
$$\ell_b = +M_{x_b} \quad m_b = +M_{y_b} \quad n_b = +M_{z_b}$$

(Note the possible nomenclature ambiguity of the wind-oriented yaw moment, YM and the body-oriented y-direction force Y.) When $\phi = 0°$, converting from the wind-oriented forces to body-axis forces is achieved by the rotation

$$\begin{bmatrix} -A \\ +Y \\ -N \end{bmatrix} = \begin{bmatrix} \cos\psi\cos\theta & \sin\psi\cos\theta & -\sin\theta \\ -\sin\psi & \cos\psi & 0 \\ \cos\psi\sin\theta & \sin\psi\sin\theta & \cos\theta \end{bmatrix} \begin{bmatrix} -D \\ +S \\ -L \end{bmatrix} \tag{2.3}$$

The same rotation matrix is use to transform moments from wind- to body-oriented coordinates. For the moments, RM, PM and YM replace $-D$, S and $-L$, while ℓ_b, m_b and n_b replace $-A$, Y and $-N$. Transformation to stability axes follows the same procedure with θ set to zero.

3. STANDARD PROCEDURE FOR EXPERIMENT AND DATA ANALYSIS

Aerodynamic force and moment data are used for performance estimation and assessment of stability derivatives for the vehicle. As such, the accuracy of final, corrected data is extremely important. In Section 4, wall corrections to force and moment data are applied according to the approach outlined by Barlow et al. for a typical tare and interference test to illustrate the effect on the resulting aerodynamic response. The first step in the sequence is to remove gravity effects using corresponding wind-off data. Next, blockage corrections to the dynamic pressure are applied, followed by the subtraction of support T&I effects. The final step in the data analysis procedure is to apply wall corrections for streamline curvature and normal downwash. Each step of the process is described below. A few minor changes were made to the conventional approach in order to improve efficiency and to make the corrections more consistent with aerodynamic theory. The two principal differences are:

- Gravity effects (tares) are subtracted prior to removal of support effects and are calculated through a model-fitting procedure.
- Both the lift and drag force are corrected for alignment, rather than only the drag force.
- Induced angles of attack due to streamline curvature and normal downwash do not contribute to α_c.

The analysed data is insensitive to the position of the static-tare-removal step, so this alteration will not be discussed in detail. The latter two changes, however, will be discussed further in Section 5.

3.1 Static Tare Removal

For a given configuration, a wind-off pitch sequence is followed by an identical wind-on sequence. In order to save time during wind tunnel tests, a mathematical model was developed to describe the motion of a point-mass – the model's center of gravity (CG) – with an arbitrary initial position that then moves through a yaw angle ψ followed by a pitch angle θ. The wind-frame forces due to the model weight are constant, so:

$$\vec{M}_{\mathrm{BMC}}^{(W)} = \vec{r}_{\mathrm{BMC/CG}}^{(W)} \times \vec{F}_{\mathrm{CG}}^{(W)}$$

In the above notation, BMC/CG denotes r is a vector from the BMC to the model CG, and (W) denotes a vector is in the wind frame. $\vec{F}_{\mathrm{CG}}^{(W)}$ is the force vector acting at the model CG, $\vec{F}_{\mathrm{CG}}^{(W)} = [0 \;\; 0 \;\; +W_m]^{\mathrm{T}}$, where W_m is the weight of the model. The LSWT external balance turntable also has a center of gravity that is located at a point (x_1, y_1, z_1) relative to the BMC. As the turntable rotates through yaw angle ψ, it provides a similar contribution to resulting moment. It is convenient to define two intermediate coordinate systems: one model-fixed (M) and one balance-fixed (B). The position of the model CG is constant in the model frame:

$$\vec{r}_{\mathrm{BMC/CG}}^{(M)} = const = \begin{bmatrix} x_0 \\ y_0 \\ z_0 \end{bmatrix}^{(M)}$$

for a point at arbitrary position (x_0, y_0, z_0) relative to BMC (expressed in model-frame coordinates). Because both the model frame and balance frame rotate with

yaw angle ψ, a vector in the model frame is expressed in the balance frame as:

$$\vec{r}^{\,(B)} = \begin{bmatrix} \cos\theta & 0 & \sin\theta \\ 0 & 1 & 0 \\ -\sin\theta & 0 & \cos\theta \end{bmatrix} \vec{r}^{\,(M)}$$

The balance frame and wind frame differ only by yaw angle ψ. A vector in the balance frame is expressed in the wind frame as:

$$\vec{r}^{\,(W)} = \begin{bmatrix} \cos\psi & -\sin\psi & 0 \\ \sin\psi & \cos\psi & 0 \\ 0 & 0 & 1 \end{bmatrix} \vec{r}^{\,(B)}$$

If the model CG is displaced by angles (θ, ψ), then

$$\vec{r}^{\,(W)}_{\mathrm{BMC/CG}} = \begin{bmatrix} (x_0\cos\theta + z_0\sin\theta)\cos\psi - y_0\sin\psi \\ (x_0\cos\theta + z_0\sin\theta)\sin\psi + y_0\cos\psi \\ -x_0\sin\theta + z_0\cos\theta \end{bmatrix}$$

In practice, the external balance is "zeroed" by subtracting the forces and moments observed at $\theta = \psi = 0$ from other readings. This zeroes all force readings and offsets moment measurements so that:

$$\vec{M}^{\,(W)}_{\mathrm{BMC}} = W_m\mathbf{R_m} + W_t\mathbf{R_t}$$

where

$$\mathbf{R_m} = \begin{bmatrix} (x_0 \cos\theta + z_0 \sin\theta)\sin\psi + y_0(\cos\psi - 1) \\ -[(x_0 \cos\theta + z_0 \sin\theta)\cos\psi - y_0 \sin\psi - x_0] \\ 0 \end{bmatrix}; \mathbf{R_t} = \begin{bmatrix} x_1 \sin\psi + y_1(\cos\psi - 1) \\ -[x_1(\cos\psi - 1) - y_1 \sin\psi] \\ 0 \end{bmatrix}$$

At this point, some of the cumbersome notation will be dropped. The first and second components of $\vec{M}^{(W)}_{\mathrm{BMC}}$ will be denoted RM (rolling moment) and PM (pitching moment), respectively. Additionally, some simplifications to the above expression are made using the following substitutions:

$$\begin{array}{lll} M_0 = \ell_0 W_m & M_1 = \ell_1 W_t & \overline{RM_0} = W_m y_0 + W_t y_1 \\ x_0 = \ell_0 \cos\theta_0 & x_1 = \ell_1 \cos\psi_1 & \overline{PM_0} = -(W_m x_0 + W_t x_1) \\ y_0 = \ell_0 \eta_0 & y_1 = \ell_1 \sin\psi_1 & \\ z_0 = \ell_0 \sin\theta_0 & & \end{array}$$

The final result is:

$$RM(\theta, \psi) = (\cos\psi - 1)\overline{RM_0} + \sin\psi\{M_0[\cos(\theta - \theta_0) - \cos\theta_0] - \overline{PM_0}\} \tag{3.1}$$

$$PM(\theta, \psi) = (\cos\psi - 1)\overline{PM_0} + \overline{RM_0}\sin\psi - M_0 \cos\psi[\cos(\theta - \theta_0) - \cos\theta_0] \tag{3.2}$$

For a pitch sweep, $RM = \text{const} = 0$ since the balance is zeroed prior to the run. The pitching moment for a pitch sweep at zero yaw is:

$$PM(\theta, 0) = -M_0[\cos(\theta - \theta_0) - \cos\theta_0] \tag{3.3}$$

For a yaw sweep at zero pitch,

$$RM(0,\psi) = \overline{RM_0}(\cos\psi - 1) - \overline{PM_0}\sin\psi \tag{3.4}$$

$$PM(0,\psi) = (\cos\psi - 1)\overline{PM_0} + \overline{RM_0}\sin\psi \tag{3.5}$$

Static tare removal is then accomplished with the following procedure: First, a pitch-sweep static tare run is performed at zero-sideslip, where rolling moment is constant with varying pitch. The recorded pitching moment values from the pitch sweep are then fit to Equation 3.3, yielding estimates of the parameters M_0 and θ_0. Next, a yaw-sweep static tare run is performed at zero pitch. The pitching moment and rolling moment data are fit to Equations 3.4 and 3.5 to yield estimates of $\overline{RM_0}$ and $\overline{PM_0}$. Following this procedure, a discrepancy often appears between the values of $\overline{RM_0}$ and $\overline{PM_0}$ resulting from Equation 3.4 versus those resulting from Equation 3.5. This discrepancy is explained by considering the Taylor series representations of the sine and cosine functions.

To second order, Equations 3.4 and 3.5 reduce to

$$RM(0,\psi) \approx -\overline{RM_0}\,\frac{\psi^2}{2} - \overline{PM_0}\,\psi \tag{3.6}$$

$$PM(0,\psi) \approx -\overline{PM_0}\,\frac{\psi^2}{2} + \overline{RM_0}\,\psi \tag{3.7}$$

For small values of ψ, $\overline{PM_0}$ dominates in the RM equation, while $\overline{RM_0}$ dominates in the PM equation. In practice, the larger variation in these dominant terms results in a lower uncertainty in the outcome of the data fitting procedure. As such, the parameter $\overline{PM_0}$ is taken from Equation 3.4, and $\overline{RM_0}$ is taken from Equation 3.5.

3.2 Blockage Corrections

Once the static tare is removed, blockage corrections are applied to the upright data in the wind-oriented coordinate system. The solid blockage correction depends only on model and test section geometry. Following Barlow et al., the solid blockage correction takes the form:

$$\epsilon_{\text{sb}} = \frac{\Delta V_{\text{sb}}}{V_u} = \epsilon_{\text{sb},W} + \epsilon_{\text{sb},B} = \frac{K_1 \tau_{1,W} \mathcal{V}_{\mathcal{W}}}{C^{3/2}} + \frac{K_3 \tau_{1,B} \mathcal{V}_{\mathcal{B}}}{C^{3/2}} \tag{3.8}$$

In the above equation, K_1 and K_3 are respectively body shape factors for the wing and fuselage determined by model geometry, and $\tau_{1,W}$ and $\tau_{1,B}$ are respectively model-to-test-section ratio shape factors for the wing and fuselage, dependent on model and tunnel geometry. $\mathcal{V}_{\mathcal{B}}$ and $\mathcal{V}_{\mathcal{W}}$ are the body and wing volumes, respectively and ϵ is the incremental change in velocity – in this case, due to solid blockage (subscript sb). Finally, C is the test section cross-sectional area; $C^{3/2}$ is a representative test section volume. For the LSWT, $C^{3/2} = 561$ ft^3. From inspection, Equation 3.8 is consistent with the reasoning in Section 1, i.e., $\epsilon_{\text{sb}} \propto \mathcal{V}_{\text{model}}/\mathcal{V}_{\text{tunnel}}$. The shape factors K and τ were empirically determined, and plots are given by Barlow et al. The incremental velocity ϵ_{sb} is typically quite small. For the experiment discussed in Section 4, $\epsilon_{\text{sb}} = \mathcal{O}(10^{-3})$.

The wake blockage effect increases with increasing drag. Not accounting for strongly separated bluff-body flow, the incremental velocity due to wake blockage is computed using:

$$\epsilon_{wb} = \left(\frac{S}{4C}\right) C_{Du} \tag{3.9}$$

where S is again the wing planform area and C_{Du} is the uncorrected drag coefficient, defined for clarity as $C_{Du} = D/q_{\text{act}}S$. This equation is derived by modelling the de-

celerated wake region downstream of the wing as a source singularity. The correction to q_{act} is then:

$$q_{\text{c}} = q_{\text{act}}(1 + \epsilon_{\text{sb}} + \epsilon_{\text{wb}})^2 \tag{3.10}$$

where q_{c} is the corrected dynamic pressure. After applying corrections to the dynamic pressure, T&I effects are removed and the data is transferred to model aerodynamic moment reference center. The data is then further corrected for the presence of the test section walls.

3.3 Support Tare & Interference Removal

At this point, the support T&I data from the sequence described in Section 1 are subtracted from the corresponding upright data. This is done for all forces and moments (as opposed to just the drag force). The first step is to determine the combined tare and interference effects associated with the support strut, TI_L. For notational simplicity, let $\Delta = TI_L$. As discussed in Section 1, Δ is calculated using a direct, point-by-point subtraction of the inverted-with-image data from the inverted-without-image data. The support Δ is then subtracted (again point-by-point) from the upright-without-image data to yield "free-flight" wind tunnel data (see Figs 1.3–1.6 in Section 1). Aerodynamic moments are transferred from BMC to MRC using Equations 2.2 in Section 2 to yield "support-free," model-center forces and moments. These are then nondimensionalized using q_{c}, leaving true "uncorrected" coefficients C_{Du}, etc. Note that at this point, these coefficients are referred to as "uncorrected" because all of the wall corrections remain to be applied. The first boundary correction applied is the streamline curvature correction.

3.4 Wall Corrections

After transferring moments to the model MRC, corrections for streamline curvature and normal downwash are applied. The induced angle of attack due to streamline curvature is given by:

$$\Delta\alpha_{\text{sc}} = \tau_2 \delta \left(\frac{S}{C}\right) C_{LW} \tag{3.11}$$

where C_{LW} is the wing lift coefficient, and τ_2 and δ are factors representing boundary-induced upwash for a particular combination of model size and test section geometry. This change α affects the uncorrected lift coefficient, and the uncorrected pitching moment coefficient as a result. The effects on the lift and pitching moment coefficients are respectively:

$$\begin{aligned} \Delta C_{L,\text{sc}} &= -\frac{dC_L}{d\alpha}\Delta\alpha_{\text{sc}} \\ \Delta C_{m,\text{sc}} &= -0.25\Delta C_{L,\text{sc}} \end{aligned} \tag{3.12}$$

For this test, C_{LW} was approximated by subtracting wing-off data from full-model data, shown in Figure 3.1.

The normal downwash correction is applied in a similar manner:

$$\Delta\alpha_{\text{nd}} = \delta \left(\frac{S}{C}\right) C_{LW} \tag{3.13}$$

and

$$\Delta C_{D,\text{nd}} = C_{LW}\Delta\alpha_{\text{nd}} = \delta \left(\frac{S}{C}\right) C_{LW}^2 \tag{3.14}$$

The fully corrected angle of attack is:

$$\alpha_{\text{c}} = \alpha_{\text{g}} + \Delta\alpha_{\text{up}} + \Delta\alpha_{\text{sc}} + \Delta\alpha_{\text{nd}}$$

where α_{g} is the geometric angle of attack, i.e., the angle measured relative to a

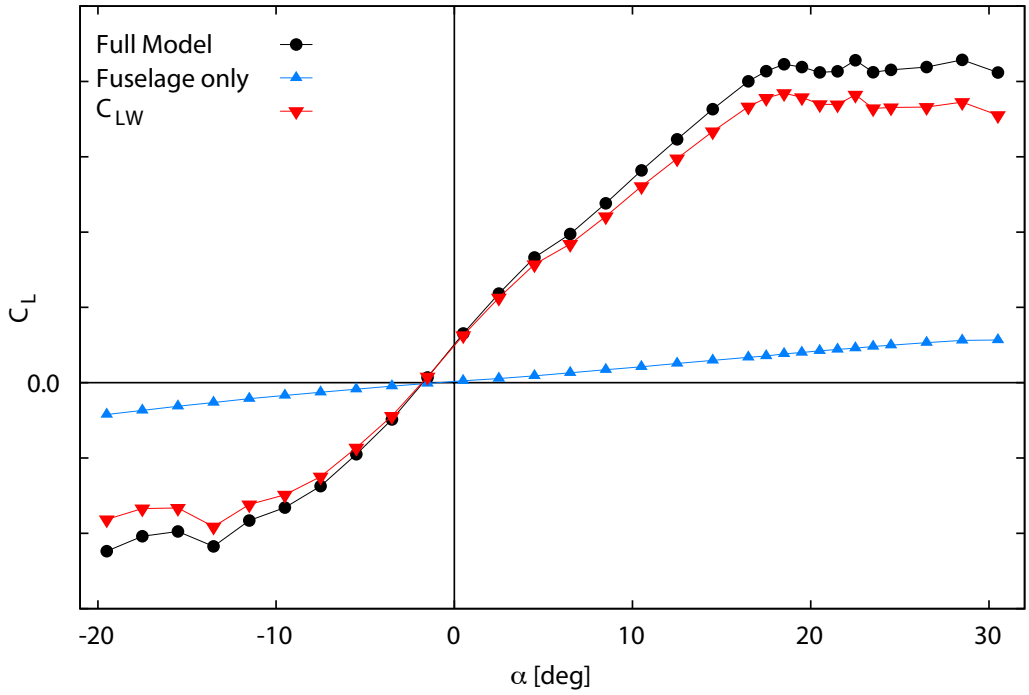

Figure 3.1: Estimate of C_{LW} using full-model and fuselage-only configurations

reference waterline using a spirit level. The uncorrected drag coefficient is then modified due to the drag induced by the test section walls:

$$C_{Dc} = C_{Du} + \underbrace{C_{LW}\Delta\alpha_{\text{up}}}_{\Delta C_{D,\text{up}}} + \underbrace{\delta\frac{S}{C}C_{LW}^2}_{\Delta C_{D,\text{nd}}} \tag{3.15}$$

In the above equation, $\Delta C_{D,\text{up}}$ and $\Delta C_{D,\text{nd}}$ are computed by approximating $\Delta\alpha_{\text{up}}$ and $\Delta\alpha_{\text{nd}}$ as small angles. The induced drag due to lift is then $L\sin\Delta\alpha \approx L\Delta\alpha$. The change in the final data resulting from this approximation is discussed further in Section 5.

The final coefficient correction is applied to pitching moment; due to the altered downwash component, the tail is at a different angle of attack than it would be in

free flight. This correction is computed using:

$$\Delta C_{m,\mathrm{CG}} = -\left(\frac{\partial C_{m,\mathrm{CG}}}{\partial \delta_s}\right)\Delta\alpha_{\mathrm{tail}} \tag{3.16}$$

In the above equation, the induced angle $\Delta\alpha_{\mathrm{tail}}$ is identical to $\Delta\alpha_{\mathrm{sc}}$ mentioned earlier, except that the factor τ_2 is determined using tail geometry rather than $c/4$. $\partial C_{m,\mathrm{CG}}/\partial\delta_s$ is the rate of change of pitching moment with respect to the tail stablizer-incidence angle. Since the change in pitching moment due to stabilizer deflection is unknown a priori, a run sequence with varying stabilizer incidence was conducted to determine the tail effectiveness $\partial C_{m,\mathrm{CG}}/\partial\delta_s$. Again, Barlow et al. contains the figures used to determine all the empirical factors in the above equations.

4. EXAMPLE APPLICATION TO A TARE & INTERFERENCE TEST

4.1 Introduction

The Oran W. Nicks LSWT is capable of performing a wide variety of aerodynamic testing. Apart from aerospace vehicles, offshore structures such as oil platforms and ships are tested by matching relevant flow and geometry conditions. Blockage corrections are applied for all applications, but the remaining wall corrections only apply to vehicles generating lift. Furthermore, the T&I strategy discussed in Section 3 is typically reserved for strut-mounted models rather than for sting- or floor-mounted models.

The LSWT was recently contracted to collect data for a twin-engine aircraft in multiple configurations. Because this was a proprietary test, no specific details will be given about the actual vehicle. Applied forces and moments were measured using the LSWT external balance for pitch angles α ranging from $-20°$ to $+30°$ and yaw angles β between $\pm 30°$ at a nominal dynamic pressure q_{act} of 95 psf. Including blockage corrections, this corresponds to an approximate flow speed of 290 ft/sec. An extensive test schedule was executed which included inverted, inverted-with-image and upright model configurations necessary for tare and interference removal. Upright-with-image configurations were also tested to establish the upflow angle. Accurate execution of this method requires the main support strut to penetrate either the top or bottom fuselage surface and that the model pitch point be such that the installed model is symmetric about the wind-tunnel midplane (which is also the location of the balance reference center). Most critical is that the distance between the model floor and image strut fairing in the inverted orientation is equal to the distance between the model floor and the main strut fairing in the upright

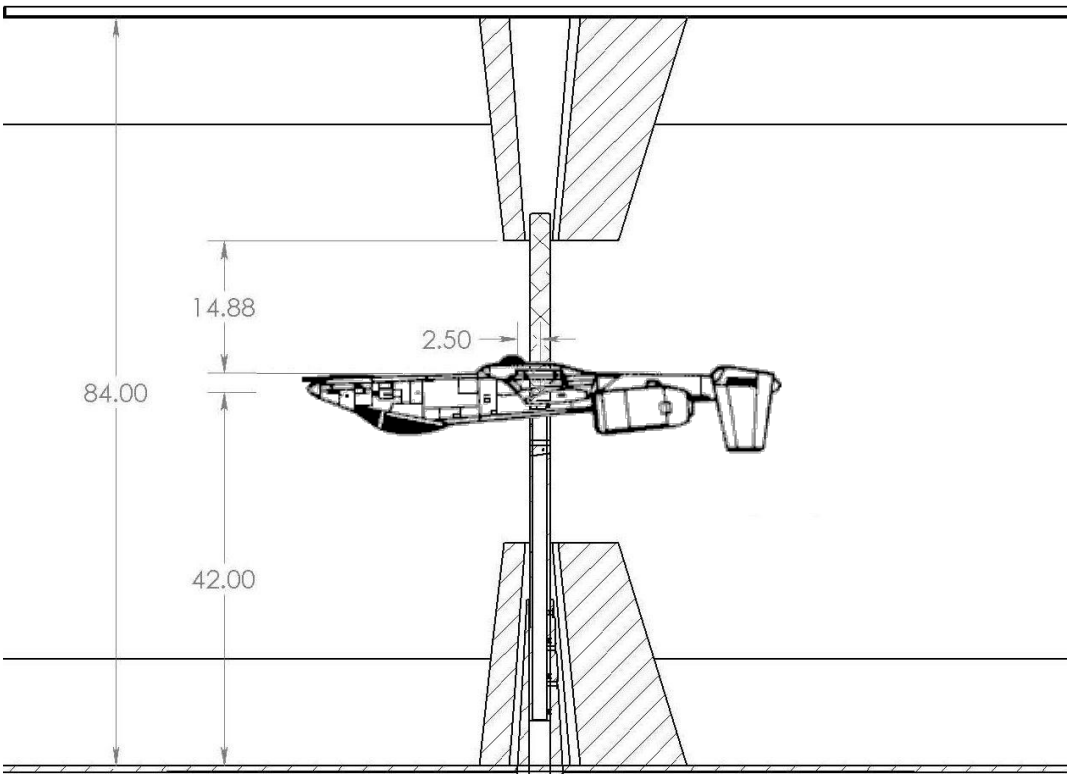

Figure 4.1: Mounting dimensions for LSWT T&I test (shown with generic model image).

configuration. Figure 4.1 shows the relevant dimensions for the inverted-with-image configuration. When the model is upright, the key dimension to match is the 14.88-inch offset between the ventral surface and the horizontal face of the strut fairing.

4.2 Model Description

The aircraft model used in the wind-tunnel test was fabricated at the LSWT using drawings supplied by the customer. The model's main component is an aluminum fuselage machined on CNC mills, assembled and hand finished. To accommodate a drag build-up study, many of the removable model components had close-outs that gave a smooth outer model surface when the component of interest was removed. Depending on the part, these add-on components were fabricated of aluminum using

the CNC mill or were fabricated of rapid-prototyper (RP) resin using one of several RP machines at the LSWT. Bolt holes were filled with model clay and seams were covered with aluminum tape.

The overall model length is approximately 62 inches measured from the nose to the aftmost point on the tail in a waterline plane. The overall wingspan is 70 inches, and the wing is rectangular and unswept. In the middle of the fuselage, the main aluminum body is approximately 10 inches wide.

4.3 Experimental Setup

The model was mounted to a 2.25-inch diameter annular steel strut connected to the external balance; the center of the strut provided a data channel for internal instrumentation to reach the data acquisition (DAQ) system below the test section. The portions of the struts exposed to the flow were knurled during manufacturing to trip turbulent transition and minimize Reynolds number effects (see Figure A.2 in Appendix A). The image strut was the same outer diameter as the main strut, but was not attached to the test section walls so as to directly measure the tare and interference effects of the ventral strut. Both struts were shielded from the flow by 25-inch-tall fairings shaped as symmetric tapered airfoils which were designed to match the 14.88-inch offset from the model's ventral surface. The main-strut fairing was attached to the LSWT upper turntable, which was maintained in a fixed position throughout the test. With this setup, the lower turntable is able to provide yaw motion while the fairing attached to the upper turntable remains at a 0° angle of attack relative to the flow. Clearance of approximately 0.25 inches between the struts and fairings ensure that the entire model load passes through the external balance. Fouling circuits ensure the load path is not compromised during testing.

An internal Exlar GSX40-0401 linear actuator (Appendix A) mounted between

the model and strut allowed a commanded pitch attitude while maintaining attitude and resisting applied loads. The GSX40 features a roller screw mechanism which maintains precise positioning under larger loads and an internal brake which enables the decoupling of the actuator from the electrical system once position is attained. These were favorable features as the actuator showed virtually no displacement from the desired attitude while under load, nor did it contribute to any signal noise. An electronic inclinometer with 0.05° accuracy inside the model provided pitch-angle feedback throughout the test.

The model was installed into the test section through the removable ceiling using an overhead hoist. The main strut was installed followed by the lower fuselage half, which mounts to the main strut using the linear actuator. Following this, an optical transit located downstream of the model was used to bring the model to zero yaw and zero the wind-tunnel turntable. Before testing, a large load was placed on the nose of the model to test pitch actuator rigidity. Virtually no play was observed, proving the system to be suitably stiff. Removable sliding seals were installed to mitigate flow-through for each run. Free motion of the sliding seals was promoted by lightly sanding key portions of the knurled struts.

4.4 Pitch and Yaw Sweeps

The main activity of the test program consisted of pitch and yaw sweeps during which external balance data were recorded. Pitch sweeps were performed across a range $\alpha = -20°$ to $+30°$, always at $\beta = 0°$. Yaw sweeps were performed across a range $\psi = \pm 30°$ in $2°$ increments. These were typically executed at pitch angles $\alpha = 0°$, $6°$ and $14°$. Before a sequence of sweeps for any new configuration, the external balance was zeroed at model attitude $\alpha = \beta = 0°$. Two static tare runs were executed for each significant model configuration; one pitch sweep at $\beta = 0°$ and

one yaw sweep at $\alpha = 0°$. A configuration was deemed 'significant' if the addition or removal of a component would greatly alter the overall weight and/or center of gravity location of the model. A non-linear least squares fit was then applied which defined the behavior of the load response for a yaw sweep at any pitch angle. The static tare data were then subtracted from wind-on data to yield only aerodynamic forces and moments, using the procedure described in Section 3.

For a pitch sweep, data were taken first with wind off and the model oriented at $\alpha = \beta = 0°$. Next, the flow was brought to speed with $q_{\text{act}} = 95$ psf. Calibration between q_{set} and q_{act} as discussed in Section 2 last occurred in July 2011. With wind on and an initial $\alpha = \beta = 0°$ data point recorded, the model was moved through a pitch sweep while recording a data point at each prescribed pitch angles. Pitch sweeps incremented 2° between each point. For consistency, the model nose swept from test section floor to ceiling in the upright configuration (θ moving from negative to positive) and from ceiling to floor in the inverted orientation. The highest angle of attack was $\alpha = +30°$. After recording this point, the model was returned to $\alpha = 0°$ for a final wind-on data point. Then, wind speed was brought to zero and a final wind-off data point was recorded at $\alpha = 0°$.

The procedure was similar for yaw sweeps. Yaw sweeps were always conducted with body-fixed sideslip angle β starting at $+30°$ and sweeping to $-30°$. For upright runs, this meant that ψ swept from negative to positive (the converse being the case for inverted runs). The model was brought to the appropriate pitch attitude and a wind-off data point was recorded at $\psi = 0°$. Next, the tunnel was brought to q_{act} = 95 psf and a wind-on point was recorded at the same attitude. The model was then moved to $\beta = +30°$ (wind impinging on the starboard side of the fuselage) and stepped in 2° increments to $\beta = -30°$. After recording the last wind-on data point at $\beta = -30°$, the model was returned to $\beta = 0°$ for the final wind-on and wind-off

data points. The purpose of each wind-off data point is to provide a measure of experimental repeatability.

Throughout sweeps of both types, q_{act} was continuously monitored by wind-tunnel personnel and the appropriate setting was maintained by manually adjusting fan pitch, an operation required throughout each run to ensure a constant flow rate is maintained despite the changing test section blockage. The data acquisition and experiment control program only record data when q_{act} falls within 0.15 psf of the setpoint.

Near the midpoint of the test, configurations of both inverted-with-image and upright-with-image were swept through a sequence of pitch angles to determine the balance-to-flow misalignment as discussed in Section 1. The best fit to $(C_{L,\text{upright}} - C_{L,\text{inverted}}) = 0$ is $\Delta\alpha = +0.5°$. Figures 4.2 and 4.3 show the effect of the upflow correction to angle of attack.

4.5 Experimental Data Analysis

Experimental data were analysed using the methods described in Section 3. The test section cross-sectional area $\mathcal{C}$ is 68 ft^2. The total wing volume is approximately 1.1 ft^3. The wing thickness ratio yields $K_1 \approx 1.10$ and the wing-to-tunnel span ratio $b/B = 48\%$ yields $\tau_{1,W} \approx 0.865$ for tunnel span-to-height ratio $B/H = 1.43$. The velocity increment due to wing blockage is then $\epsilon_{\text{sb},W} = 1.7 \times 10^{-3}$. The model fuselage volume is 1.48 ft^3 with geometry yielding $K_3 \approx 0.932$. The fuselage-to-tunnel span ratio $b/B = 0$ (for a body of revolution) yields $\tau_{1,B} \approx 0.865$ for tunnel span-to-height ratio $B/H = 1.43$. The incremental velocity due to fuselage blockage is $\epsilon_{\text{sb},B} = 2.1 \times 10^{-3}$. The total velocity increment due to solid blockage is:

$$\epsilon_{\text{sb}} = \frac{\Delta V_{\text{sb}}}{V_u} = \epsilon_{\text{sb},W} + \epsilon_{\text{sb},B} = 3.8 \times 10^{-3}$$

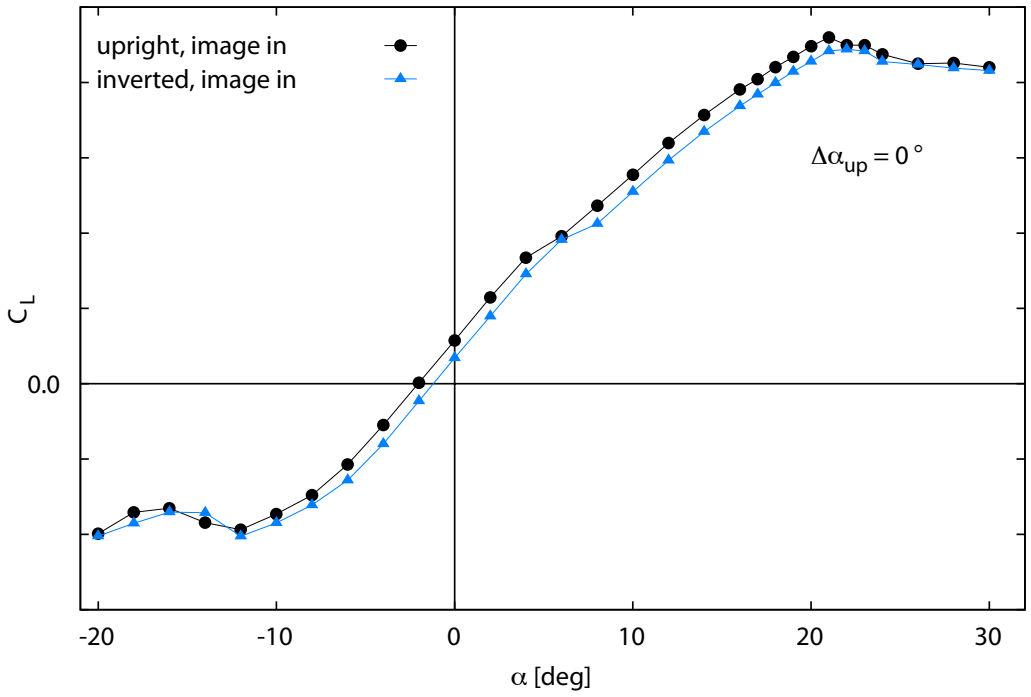

Figure 4.2: Upright and inverted C_L data, unaligned

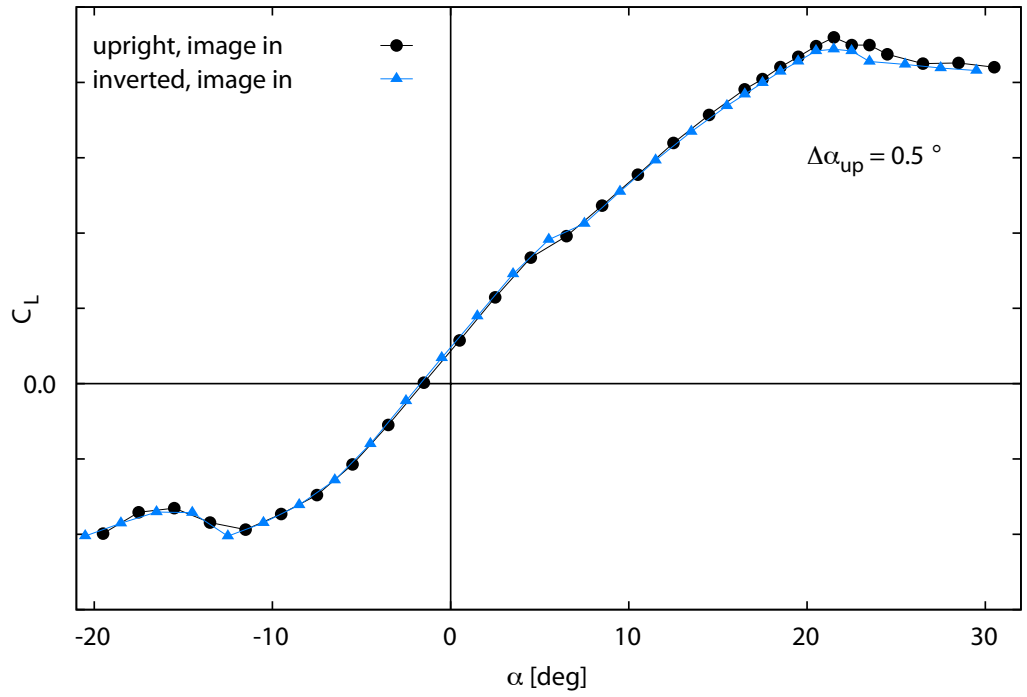

Figure 4.3: Upright and inverted C_L data, aligned with $\Delta\alpha_{\text{up}} = 0.5^\circ$

Wake blockage also affects the dynamic pressure, but is proportional to the drag force:

$$\epsilon_{\text{wb}} = \frac{1}{4\mathcal{C}q_{\text{act}}} D \approx 3.9 \times 10^{-5} \text{ lb}_f^{-1} \cdot D$$

The blockage-corrected dynamic pressure experienced by the model is calculated from Equation 3.10 repeated below:

$$q_c = q_{\text{act}}(1 + \epsilon_{\text{sb}} + \epsilon_{\text{wb}})^2$$

Following the correction to dynamic pressure, the support Δ is removed using the process outlined in Section 1.

The downwash correction factor $\tau_2 = 0.05$, determined using $l_t/B \approx 2\%$, $k = b/B = 48\%$ and $\lambda = H/B = 0.7$. The boundary correction factor $\delta = 0.1125$, computed for a closed octagonal jet using the same values for k and λ. The lift and pitching moment coefficients are then incremented using Equations 3.12. The normal downwash correction is applied using Equations 3.13 and 3.14 with the same value of δ used in the streamline curvature correction. Finally, the tail-upwash correction is applied using Equation 3.16; for this application, τ_2 is determined with $l_t/B = 23\%$ so that $\tau_2 = 0.6$.

Ultimately, the objective is to obtain performance and stability data of a free-air vehicle. Figure 4.4 shows the effect of T&I removal and application of moment transfers and boundary corrections. The decreasing effect of T&I-removal can be seen at high angles of attack, and a discrepancy in negative-stall angle appears near $C_{L,\text{min}}$. The latter phenomenon may result from the angle of attack bias discussed above. This concept will be explored further in Section 5.

Appendix B contains tables listing key constants and reference dimensions dis-

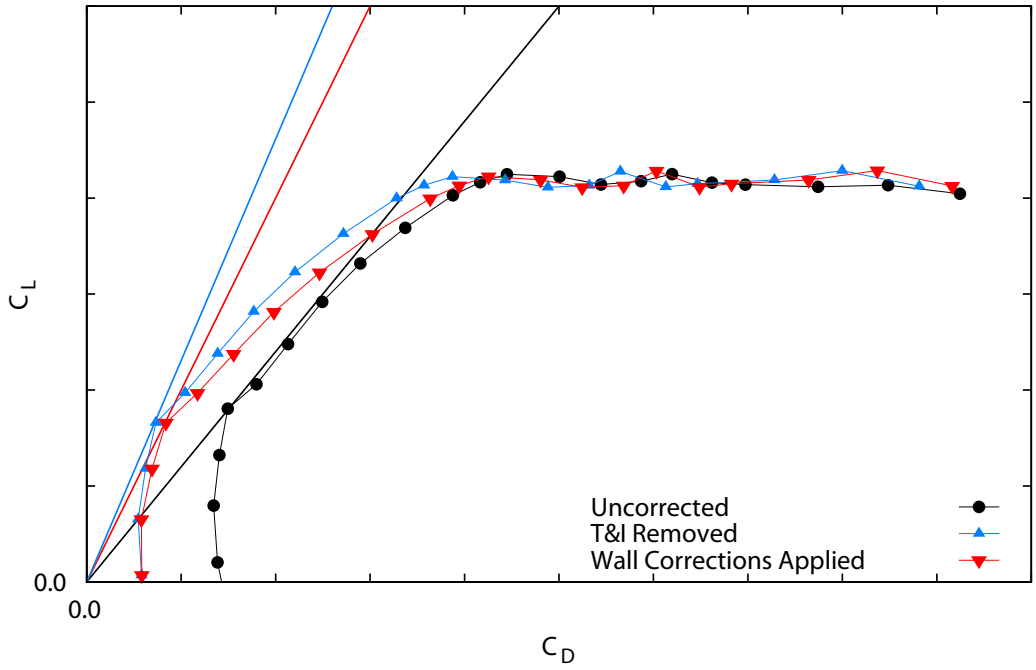

Figure 4.4: Effect of corrections on maximum L/D

cussed in the preceding sections. The six wind-frame forces and moments are transferred to other reference frames following the application of the wall corrections. Model-frame force and moments are calculated with Equation 2.3.

5. UNCERTAINTY ANALYSIS AND ERROR PROPAGATION

Section 3 focused on the conventional method for analysing aerodynamic measurements obtained during a wind tunnel tare and interference test. As mentioned earlier, the procedure as given by Barlow et al. makes use of approximations which may introduce avoidable errors into the final aerodynamic force and moment data. Estimating these errors is the objective of this section. The principles of uncertainty analysis are first introduced, followed by an examination of the uncertainty present in the external balance measurements and the data reduction procedure for a tare and interference test with boundary corrections. Recommendations will be made as to whether the approximations made in the current approach lead to an unacceptable amount of error.

One of the caveats of measuring a physical system is that the experimenter can never be completely confident that the resulting measurement values are the "true" measurement values; indeed, if the true values were known a priori, there would be no purpose to the experiment. Illegitimate errors, which arise from experimental mistakes such as misread instrumentation, will not be considered in this thesis. Instead, the focus will be on random fluctuations in measurements and on model and systematic errors that limit the precision and accuracy of the final result.

5.1 Overview of Uncertainty Analysis Techniques

It is important to first note the distinction between accuracy and precision. Bevington and Robinson [6] define accuracy as the proximity of an experimental result to its true value. Precision, however, is a measure of how well a result was determined, i.e., the repeatability of a result without reference to its true value. As one may expect, the overall "goodness" of a result depends on both high accuracy *and*

precision. The term "uncertainty" refers to the precision with which a result is determined. Because the true aerodynamic values are not known a priori, the *actual* error is unknown. As such, it is necessary to develop a consistent method for determining and quoting the estimated error.

Bevington and Robinson make another distinction between systematic error and random error. Systematic error describes repeatable errors that cause the measured result to differ from the true result. Faulty calibrations and observation bias are two examples of systematic errors. Model form errors are another type of systematic error and arise when modifications are applied to precise wind tunnel data. Despite potentially perfect measurements of aerodynamic loads, the transformation from wind tunnel data to free-air data may introduce additional error.

Random errors are typically assumed to follow a Gaussian distribution. Considering a generic function $x(u, v)$, the difference between the true value of x and its estimate based on uncertain measurements of u and v can be estimated using a first-order Taylor-series expansion:

$$x_{\text{est}} - x_{\text{true}} = \frac{\partial x}{\partial u}(u_{\text{meas}} - u_{\text{true}}) + \frac{\partial x}{\partial v}(v_{\text{meas}} - v_{\text{true}}) \tag{5.1}$$

The above expression quantifies the departure of the estimated value of x from its true value based on its sensitivity to u and v.

In practice, the actual differences on the right-hand side are replaced with uncertainties because true values are unknown. Furthermore, to ensure the propagated uncertainty on x is positive and to account for the possibility that errors in u and v are correlated, Equation 5.1 is squared to yield:

$$\sigma_x^2 = \sigma_u^2 \left(\frac{\partial x}{\partial u}\right)^2 + \sigma_v^2 \left(\frac{\partial x}{\partial v}\right)^2 + 2\sigma_{uv}^2 \left(\frac{\partial x}{\partial u}\right)\left(\frac{\partial x}{\partial v}\right) \tag{5.2}$$

The term σ_{uv}^2 is the statistical representation of how errors in u and v are correlated, known as the covariance (which can be positive or negative). Equation 5.2 propagates measured uncertainties σ_u, σ_v, and their covariance σ_{uv}^2 into the resulting uncertainty σ_x. The covariance terms are often uncorrelated or are small in relation to the other terms and are ignored for the following discussion. In this case, the error propagation formula reduces to:

$$\sigma_x^2 = \sum_i \sigma_{u_i}^2 \left(\frac{\partial x}{\partial u_i} \right)^2 \tag{5.3}$$

5.2 Measurement Uncertainty In Wind Tunnel Testing

Measurement uncertainty is first introduced into any measurements taken due to random error. The external balance is calibrated periodically, and load checks are routinely performed during operation. The load checks hang a known weight from a known location in order to generate six known forces and moments. The balance is zeroed prior to a data run with the model in its starting position (usually $\theta = \psi = 0°$). The force and moment measurement uncertainties σ_F and σ_M are the greater of:

$$\sigma_F = 0.2 \text{ lb}_\text{f} \text{ or } 0.2\% \quad \text{and} \quad \sigma_M = 0.2 \text{ ft} \cdot \text{lb}_\text{f} \text{ or } 0.2\%$$

In many cases, uncertainty due to random error is approximated as the root-mean-squared error (rmse):

$$\text{rmse} = \sqrt{\frac{\sum_{n=1}^{N} (y_n - \hat{y}_n)^2}{N}} \tag{5.4}$$

After wind-off data are obtained, the flow is brought to speed and the model is set to an attitude θ, ψ. The test section dynamic pressure q_act is calulated from q_set through the calibration mentioned beforehand. From Hidore, the measurement un-

certainty in q_{act} is 0.02 psf. The pitch angle θ is routinely verified, first with a digital inclinometer and again if necessary with a bubble clinometer. These instruments are placed on a surface parallel to waterline zero (WL 0) with the linear actuator set zero pitch. For this wind tunnel entry, a digital inclinometer was also mounted inside the model to provide constant pitch-angle feedback throughout the test. Figure 5.1 shows pitch-angle feedback for the T&I runs. The rmse for this case was 0.004°, far smaller than instrument's bias error. As such, a conservative estimate of the uncertainty in α_g is 0.1°, which is twice the bias error mentioned in Section 4. Prior to the start of a test, the external balance turntable is aligned with the geometric center of the test section (the theoretical flow direction) using a surveyor's transit and physical markings fore and aft of the test section ceiling. The model is then aligned with the flow using the same procedure, this time with a scribe line machined down the center of the model. From Hidore, this process yields an uncertainty in model yaw angle of $\sigma_{\psi_0} = 0.05°$, where σ_{ψ_0} is the uncertainty with which zero-sideslip is set. This distinction is made because once ψ_0 is set, no verification process exists to ensure that the commanded sideslip angle is equivalent to that of the model. It is thought that the uncertainty in yaw increment $\sigma_{\Delta\psi}$ from the $\psi = 0°$ position is less than 0.1°.

5.3 Static Tare

The three forces and the yawing moment are nominally constant for a wind-off sweep in either pitch or yaw, as mentioned in the static tares discussion (Sec. 3). As such, the uncertainty in the measurement of those four aerodynamic loads remains unchanged from that discussed earlier. Figure 5.2 shows every load except F_Z remains within measurement uncertainty from zero. This may result from issues with model setup and will not be considered an additional contribution to the measurement

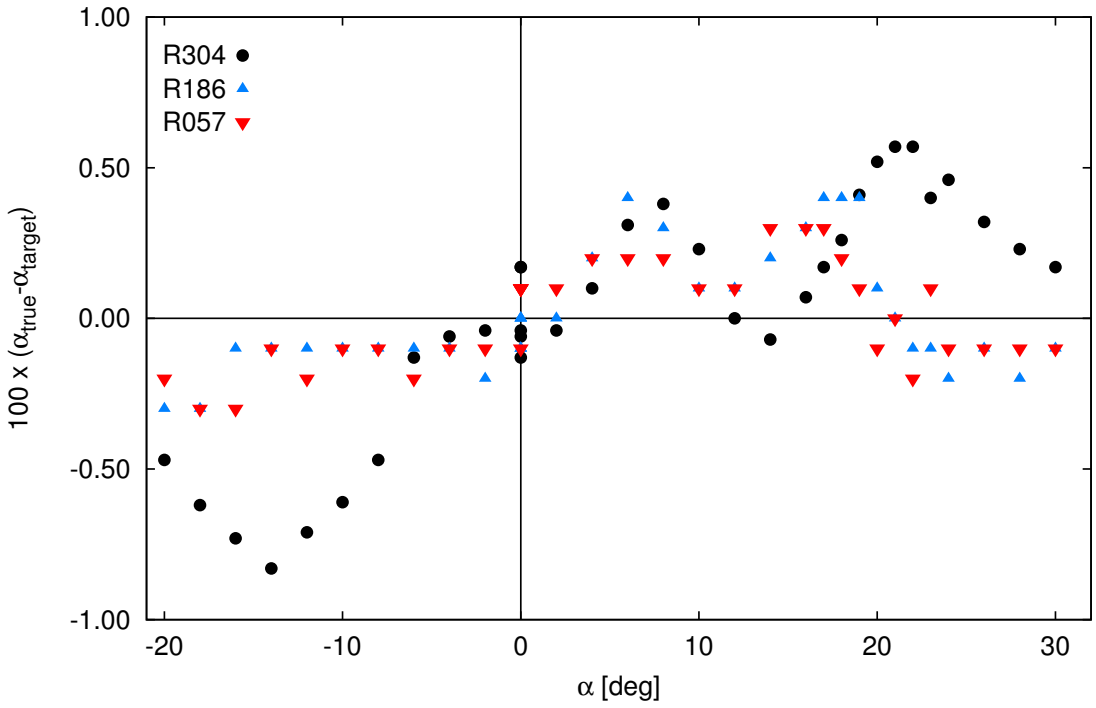

Figure 5.1: Pitch-angle feedback for T&I runs

uncertainty. The rolling and pitching moments are predicted by the mathematical model derived in Section 3. The measured moments are fit to the mathematical model, whose goodness of fit is determined using the rmse (Equation 5.4). For this application, y_n are measured values, $\hat{y}_n$ are the values predicted by M_{T}, and N is the number of data points in the pitch or yaw sweep.

The first step in the static tare procedure is a pitch sweep at zero sideslip. Pitching moment data are fit to Equation 3.3, repeated below:

$$PM(\theta, 0) = -M_0[\cos(\theta - \theta_0) - \cos\theta_0]$$

The result is shown in Figure 5.3. For this fit, $M_0 = -98$ ft·lb$_f$ and $\theta_0 = -55.6°$ which yields an rmse of 0.05 ft·lb$_f$.

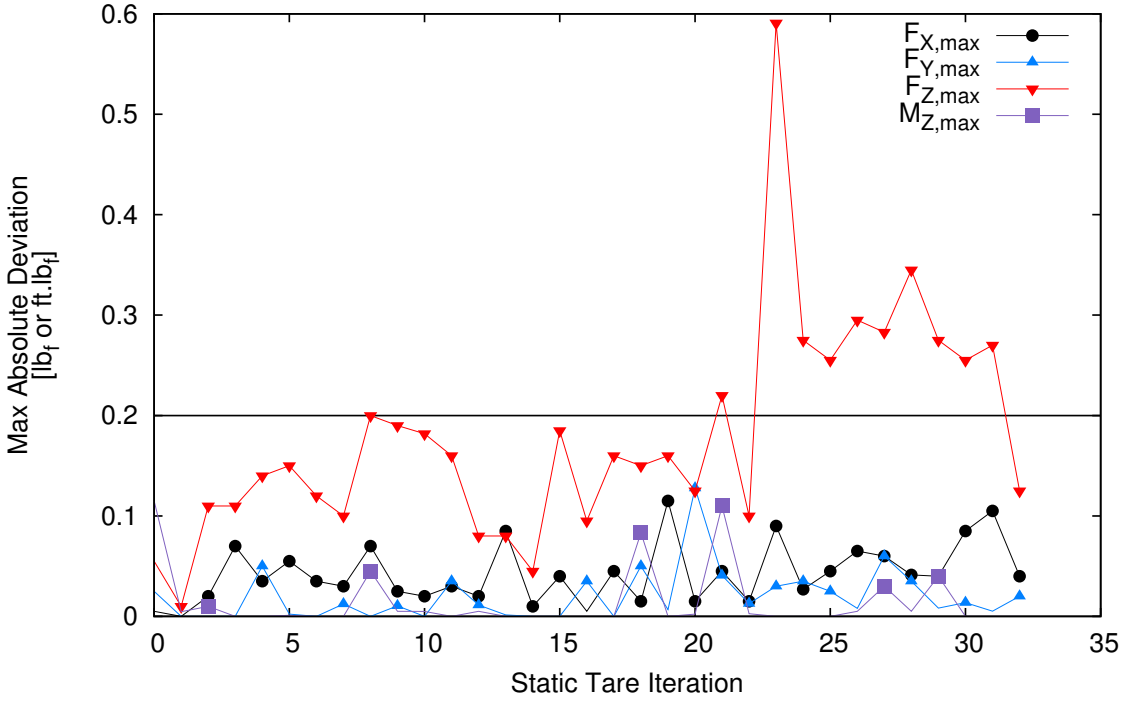

Figure 5.2: Maximum measurement fluctuations during static tare runs.

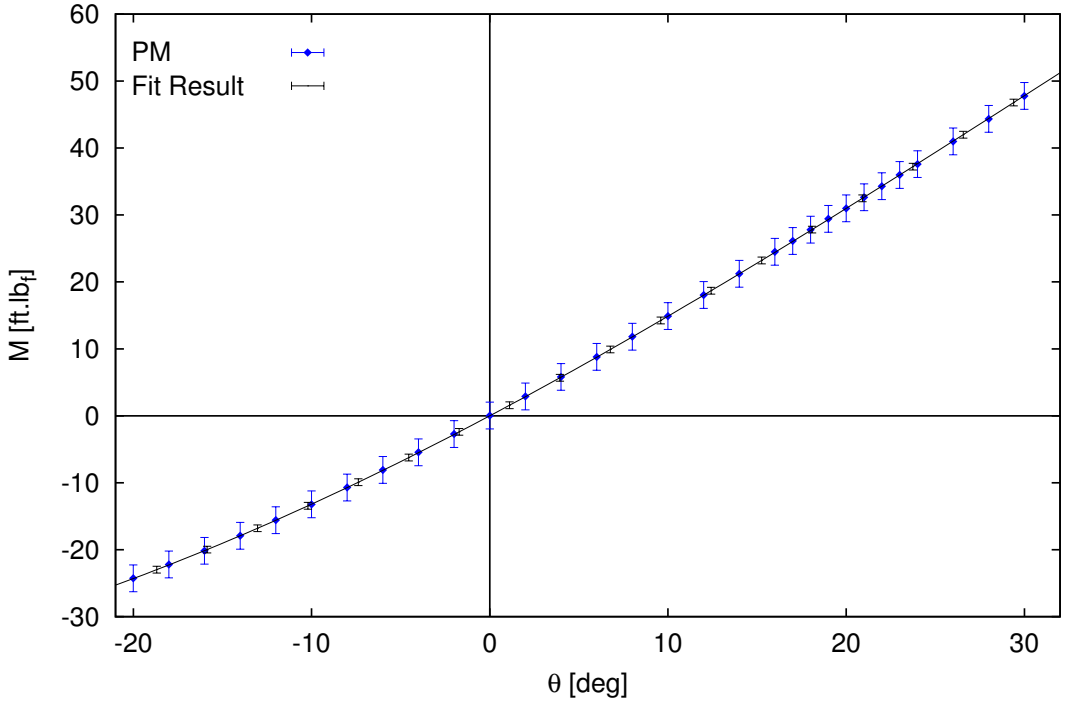

Figure 5.3: Pitch sweep static tare fit result. Error bars magnified 5x

The pitch sweep is followed by a yaw sweep at zero pitch. Rolling and pitching moment data are respectively fit to Equations 3.4 and 3.5 to yield estimates of PM_0 and RM_0. For the example shown in Figure 5.4, the coefficients computed from Equation 3.4 are $RM_0 = -276$ ft·lb$_f$ and $PM_0 = -123$ ft·lb$_f$. However, those computed from Equation 3.5 are $RM_0 = -274$ ft·lb$_f$ and $PM_0 = -137$ ft·lb$_f$. The maximum rmse for the zero-pitch yaw sweep is approximately 1 ft·lb$_f$. As discussed earlier, PM_0 dominates in Equation 3.4 and RM_0 dominates in Equation 3.5. Using $RM_0 = -274$ ft·lb$_f$ and $PM_0 = -123$ ft·lb$_f$, Equations 3.1 and 3.2 can predict the behavior of the model CG for a yaw sweep at any pitch angle between $-20^\circ \leq \alpha \leq +30^\circ$. Figure 5.5 shows the accuracy of the computed fitting function for $\theta = \alpha = 14^\circ$. The maximum rmse for the overall static tare procedure is also 1 ft·lb$_f$. Note that the error bars in Figures 5.3–5.5 are magnified by a factor of 5 in order to make them visible.

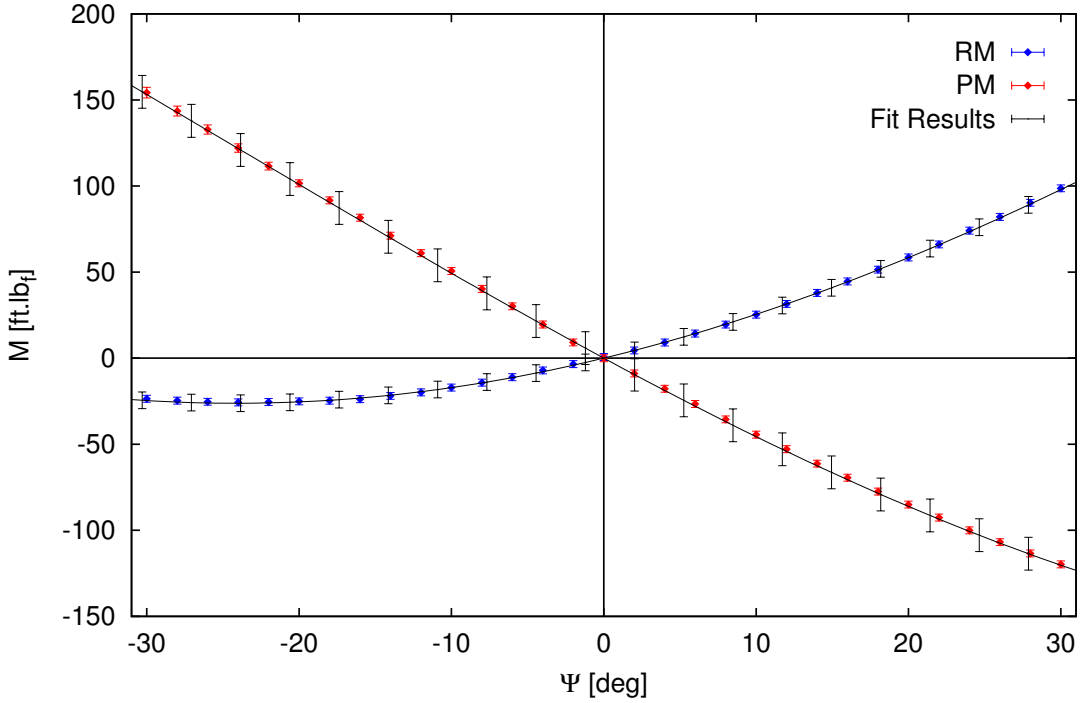

Figure 5.4: Yaw sweep static tare fit result, $\theta = \alpha = 0°$. Error bars magnified 5x

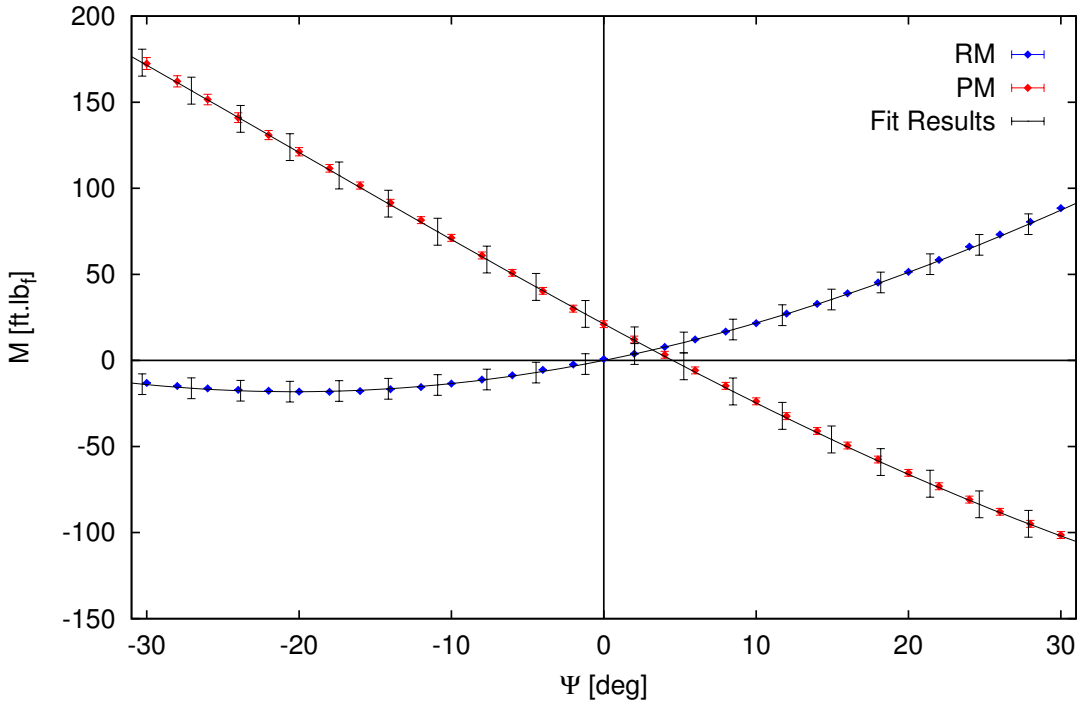

Figure 5.5: Yaw sweep static tare fit result, $\theta = \alpha = 14°$. Error bars magnified 5x

Uncorrected coefficients are computed using the blockage-corrected value of dynamic pressure q_c to scale gravity-subtracted forces and moments. For a generic force measurement F:

$$C_{Fu} = \frac{F}{q_c S} = \frac{F}{q_{act}(1+\epsilon_T)^2}$$

where $\epsilon_T = \epsilon_{sb} + D/4q_{act}C$. For $\epsilon_T \ll 1$, the binomial theorem is used to approximate the above result as:

$$C_{Fu} \approx \frac{F}{q_{act}S}(1-2\epsilon_T) = \frac{F}{q_{act}S}\left(1 - 2\epsilon_{sb} - \frac{D}{2q_{act}C}\right)$$

Similarly, for a generic moment measurement M:

$$C_{Mu} \approx \frac{M - M_T}{q_{act}S\ell}(1-2\epsilon_T) = \frac{M - M_T}{q_{act}S\ell}\left(1 - 2\epsilon_{sb} - \frac{D}{2q_{act}C}\right)$$

where M_T is the wind-off moment, and ℓ is a reference length ($\bar{c}$ for M_y and b for M_x).

Assuming exact reference dimensions S and ℓ, the uncertainty in C_{Mu} depends on the measured moment and dynamic pressure, the goodness of the static tare fit model, and on the accuracy of the blockage correction factors ϵ. ϵ_{wb} is itself sensitive to the drag force measurement D and the uncorrected dynamic pressure q_{act}. Assuming no covariance between the five variables, the uncertainty in C_{Mu} is calculated with Equation 5.3:

$$\begin{aligned}\sigma^2_{C_{Mu}} = &\left(\frac{C_{Mu}}{M - M_T}\right)^2(\sigma^2_M + \sigma^2_{M_T}) + \left[\frac{C_{Mu}}{q_{act}}\left(1 - \frac{\epsilon_{wb}}{1-2\epsilon_T}\right)\right]^2\sigma^2_{q_{act}} \\ &+ \left(2\frac{C_{Mu}}{1-2\epsilon_T}\right)^2\sigma^2_{\epsilon_{sb}} + \left(\epsilon_{wb}\frac{C_{Mu}}{1-2\epsilon_T}\right)^2\sigma^2_D\end{aligned} \tag{5.5}$$

Equation 5.5 is further simplified by examining the parenthetical term multiplying $\sigma^2_{q_{\text{act}}}$. The term $\epsilon_{\text{wb}}/(1-2\epsilon_{\text{T}})$ can be neglected because it is small compared to 1. Additionally, the term multiplying σ_D^2 can be neglected in the final result because $\epsilon^2_{\text{wb}} \sim 0$ appears in the numerator when expanded. Equation 5.5 then reduces to:

$$\left(\frac{\sigma_{C_{Mu}}}{C_{Mu}}\right)^2 = \frac{\sigma_M^2 + \sigma_{M_T}^2}{(M-M_T)^2} + \left(\frac{\sigma_{q_{\text{act}}}}{q_{\text{act}}}\right)^2 + 4\left(\frac{\sigma_{\epsilon_{\text{sb}}}}{1-2\epsilon_{\text{T}}}\right)^2 \tag{5.6}$$

From this progression, it is evident that the drag uncertainty has a negligible contribution to the uncertainty in C_{Mu}. Furthermore, because of the assumed model form error associated with the solid blockage correction, a conservative estimate for the uncertainty in the solid blockage correction factor is $\sigma_{\epsilon_{\text{sb}}} \approx \epsilon_{\text{sb}}$, i.e., the uncertainty equals the value of the correction. The final contribution to $\sigma_{C_{Mu}}$ is the uncertainty in the static tare fit procedure, to be discussed in the following section. The uncertainty in an uncorrected force coefficient C_{Fu} is found using similar logic:

$$\left(\frac{\sigma_{C_{Fu}}}{C_{Fu}}\right)^2 = \left(\frac{\sigma_F}{F}\right)^2 + \left(\frac{\sigma_{q_{\text{act}}}}{q_{\text{act}}}\right)^2 + 4\left(\frac{\sigma_{\epsilon_{\text{sb}}}}{1-2\epsilon_{\text{T}}}\right)^2 \tag{5.7}$$

From the preceding sections, σ_M and σ_F are 0.2% of the measured load and $\sigma_{q_{\text{act}}} =$ 0.02 psf. From the discussion above, $\sigma_{M_T} \approx 1 \text{ ft} \cdot \text{lb}_f$ and $\sigma_{\epsilon_{\text{sb}}} \approx \epsilon_{\text{sb}}$.

5.4 Determination of Flow Angularity

The upflow angle is determined by comparing the lift curves for the upright-with-image and inverted-with-image configurations. An elegant approach to finding this angle is to first perform a linear fit on the linear portion of the lift data for both configurations. The fitting function takes the form:

$$C_L(\alpha) \approx a_0\alpha + C_{L,\alpha=0}$$

where a_0 is the lift-curve slope and $C_{L,\alpha=0}$ is the lift coefficient at zero angle of attack. This is a straightforward operation, since the lift curve can be considered linear between the positive and negative stalled regions. The zero-lift angle of attack $\alpha_{C_L=0}$ is computed for both configurations by evaluating the quotient $C_{L,\alpha=0}/a_0$. The difference between the two zero-lift angles is twice the upflow angle. For this wind tunnel test, the unstalled portion of lift curve had two distinct slopes as shown in Figure 5.6. If the linear portions of the lift curves are split at the discontinuity occurring at $\alpha \approx 6°$, two distinct upflow angles result from the computation. This approach yields

$$\Delta\alpha_{\text{up}} = 0.42° \pm 0.03° \quad \text{or}$$

$$\Delta\alpha_{\text{up}} = 0.66° \pm 0.04°$$

Despite the low uncertainty associated with each potentially correct upflow angle, there is an approximate 0.2° discrepancy between the two upflow angles. Another approach is to fit the entire linear portion of the lift data. This predicts an upflow angle of $\Delta\alpha_{\text{up}} = 0.49°$ with an uncertainty $\sigma_{\Delta\alpha_{\text{up}}} = 0.03°$. Finally, a brute-force approach can be followed, where the rms error is defined using Equation 5.4 with $y_n = C_{L,\text{upright}}$ and $\hat{y}_n = C_{L,\text{inverted}}$. A shooting method approach is then used to determine the upflow angle as the rmse is driven to zero. This approach yields $\Delta\alpha_{\text{up}} = 0.48° \pm 0.03°$. From the preceding argument, a conservative estimate of the upflow angle is:

$$\Delta\alpha_{\text{up}} \approx 0.5° \pm 0.15°$$

The value of $\sigma_{\Delta\alpha_{\text{up}}}$ is chosen from the spread of the above results.

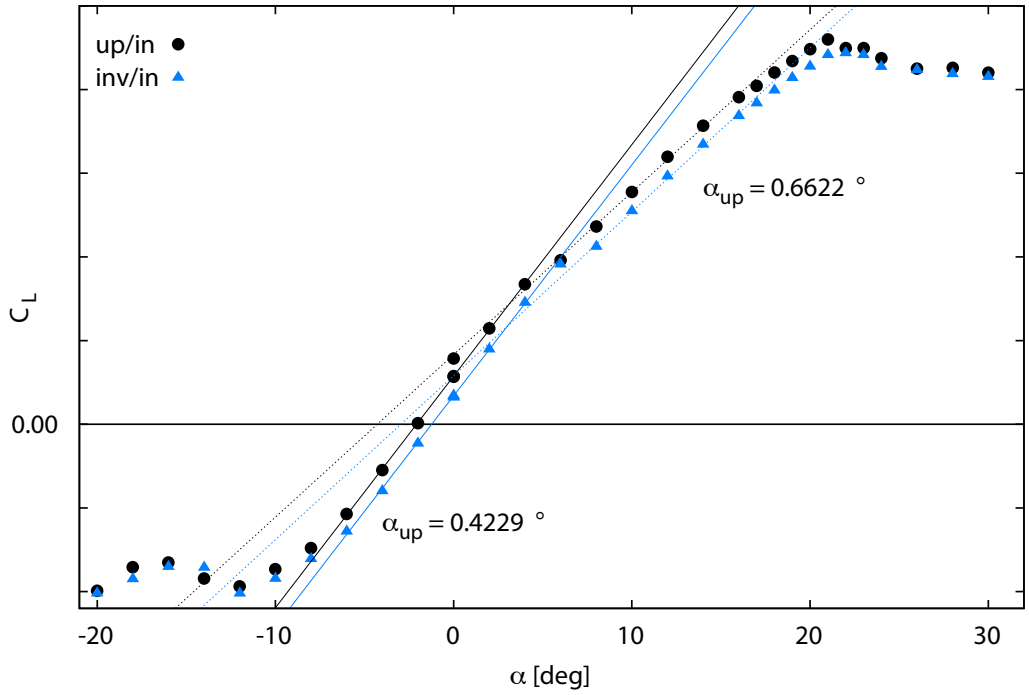

Figure 5.6: Upflow angle based on two linear fits

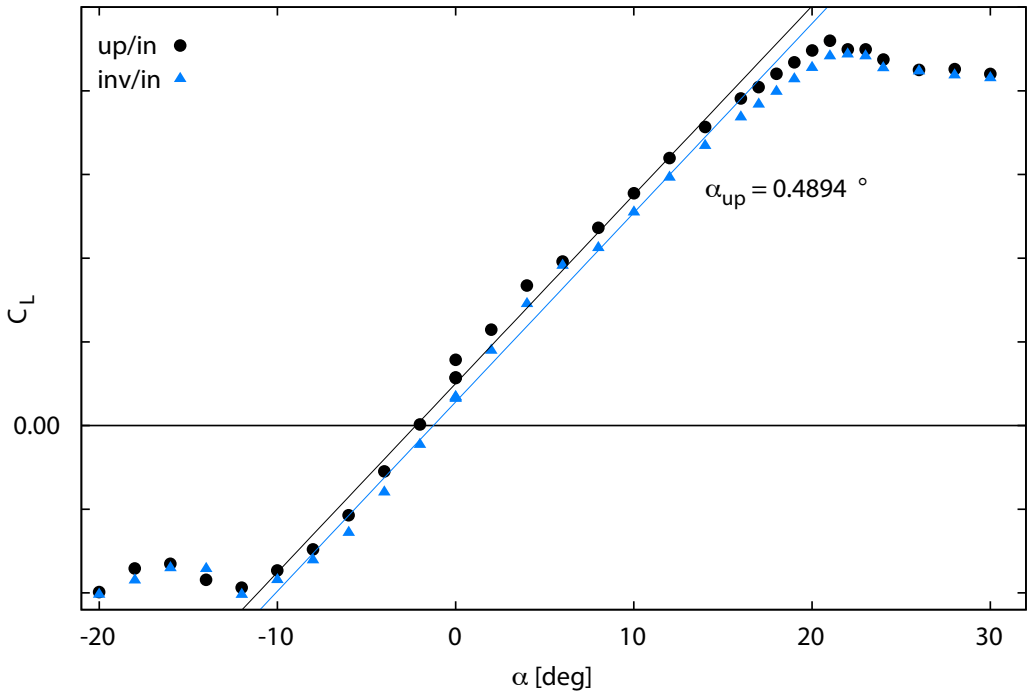

Figure 5.7: Upflow angle based on one linear fit

5.5 Support T&I Removal

Following the same procedure outlined in Section 3, support-free forces and moments are obtained by subtracting the support Δ from upright data. The procedure calls for a point-by-point subtraction to determine support strut effects. Using drag as an example, the uncorrected drag coefficient measured in wind-axis coordinates at balance-center (wabc) is computed using

$$C_{D,\text{wabc}} = C_{Du}|_{\text{upright}} - \Delta_{Du}|_{\text{inverted}} = C_{Du}|_{\text{upright}} - (C_{Du}|_{\text{inv/in}} - C_{Du}|_{\text{inv/out}})$$

The total uncertainty in $C_{D,\text{wabc}}$ is

$$\sigma_{C_{D,\text{wabc}}} = \sqrt{3}\sigma_{C_{Du}}$$

Likewise, the uncertainty for any T&I-subtracted data is $\sqrt{3}$ multiplied by the uncertainty of the relevant uncorrected coefficient.

Barlow et al. assume a point-by-point subtraction method for the support T&I correction. This could introduce error because it does not account for $\Delta\alpha_{\text{up}}$. As such, forces and moments measured at specific attitudes while inverted are subtracted from those at somewhat different upright angles of attack. Theoretically, one would mitigate this issue by first interpolating the inverted data to the upflow-corrected values of α seen by the upright data. The interpolation process introduces no additional uncertainty, as the aerodynamic forces and moments tend to vary smoothly over increments less than 1°. Additional uncertainty is however introduced when extrapolating in the post-stall region.

An interpolation scenario is shown in Figure 5.8. Here, the inverted data at $\alpha = \alpha_g - \Delta\alpha_{\text{up}}$ are interpolated to the upright angles of attack $\alpha = \alpha_g + \Delta\alpha_{\text{up}}$. The

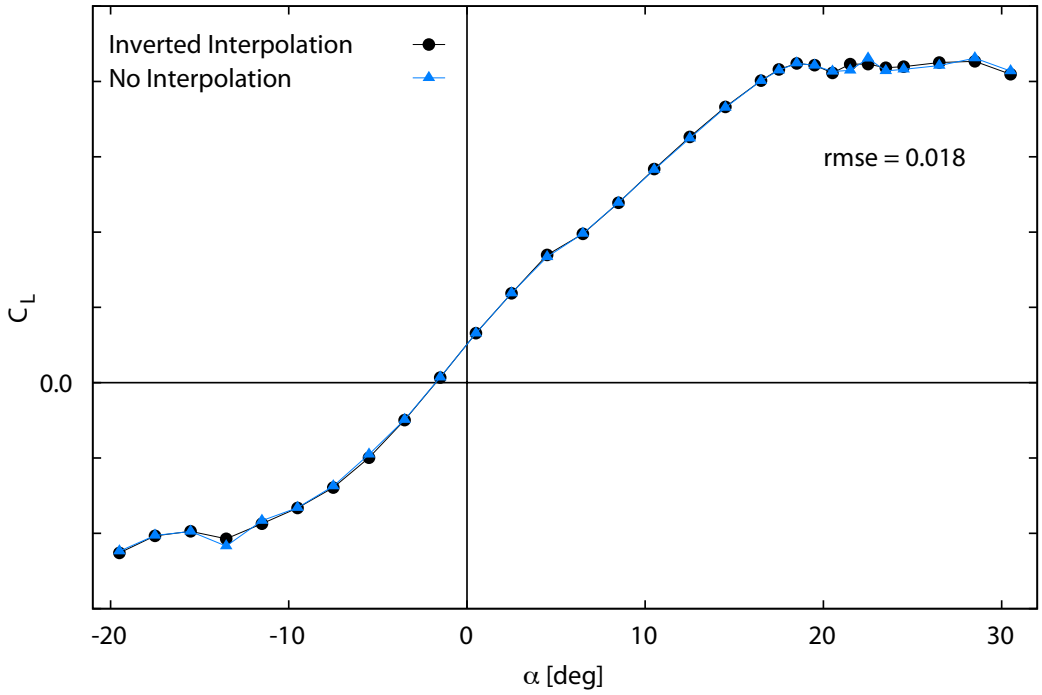

Figure 5.8: Effect of interpolation of inverted C_L data

rmse between the two C_L curves is 0.018. Figure 5.9 shows the result of the same approach for the drag data. The rmse between the two C_D curves in this case is 0.005.

Flow angularity affects yaw-sweep data as well. The effect is computed by fitting $dC_D/d\alpha$ to a generic function $f(\alpha)$. The advantage of this strategy is the ability to derive an analytic expression for $dC_D/d\alpha$ by differentiating $f(\alpha)$ with respect to α so that $f'(\alpha) \approx dC_D/d\alpha$. Figures 5.10 and 5.11 respectively show the accuracy of the $C_D(\alpha)$ and $dC_D/d\alpha$ fitting functions. A parabolic fit to $C_D(\alpha)$ results in errors of 0.023 in C_D and 0.01 in $dC_D/d\alpha$. A quartic fit to C_D results in errors of 0.012 in C_D and 0.008 in $dC_D/d\alpha$. Figure 5.11 additionally shows the largest discrepancies between the fitting functions and measured data to occur near stall.

The effect of flow alignment on $C_D(\beta)$ is derived using a first-order Taylor series

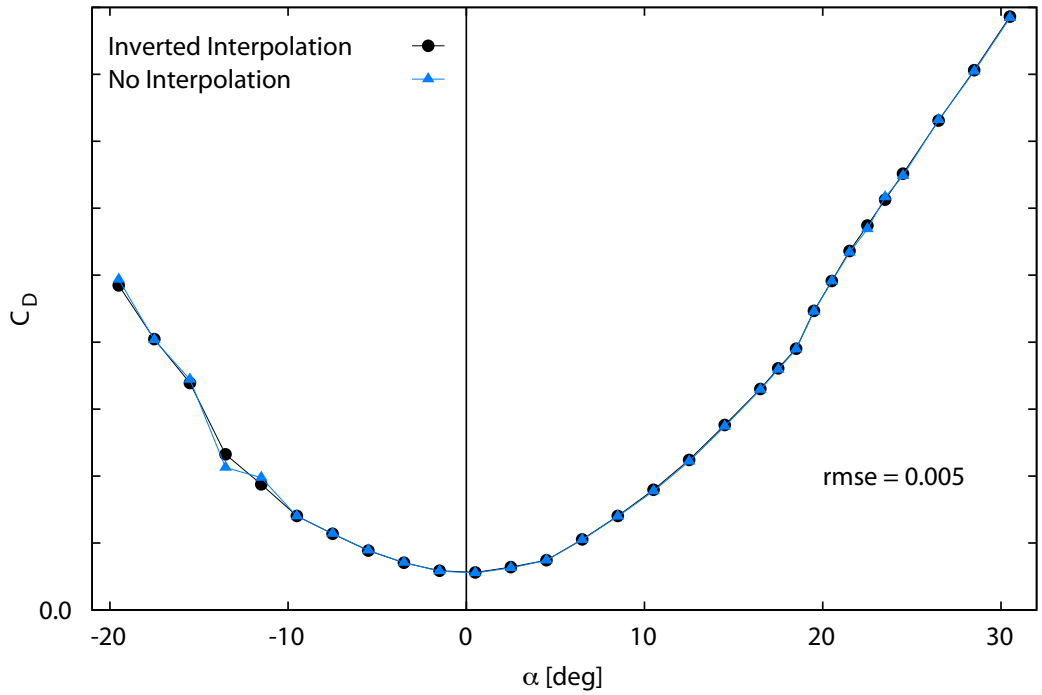

Figure 5.9: Effect of interpolation of inverted C_D data

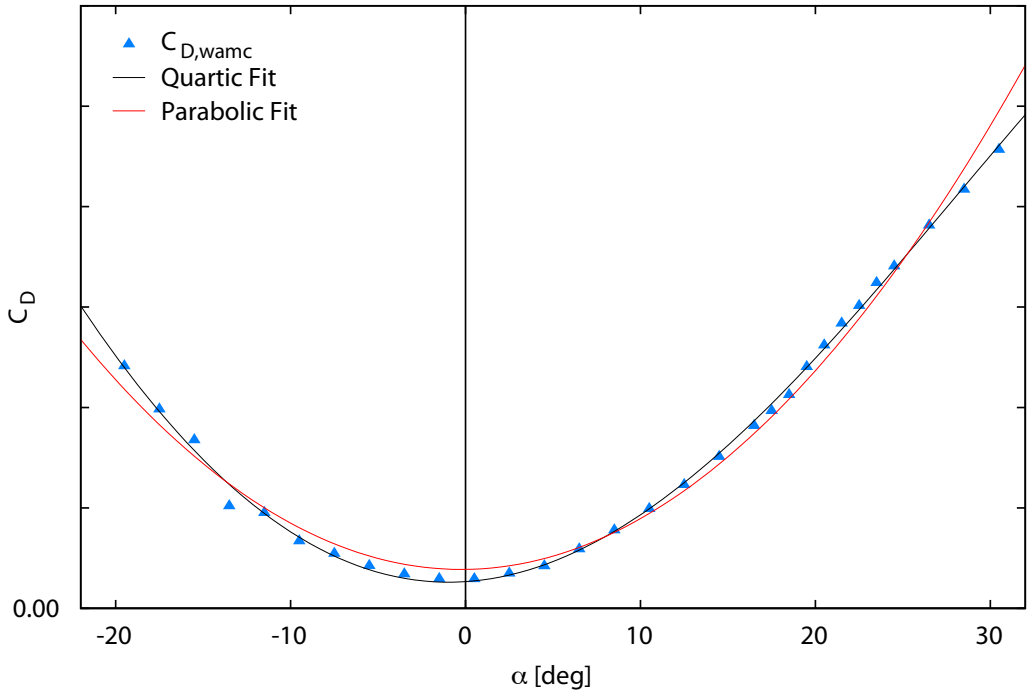

Figure 5.10: Fit result for $C_D(\alpha)$

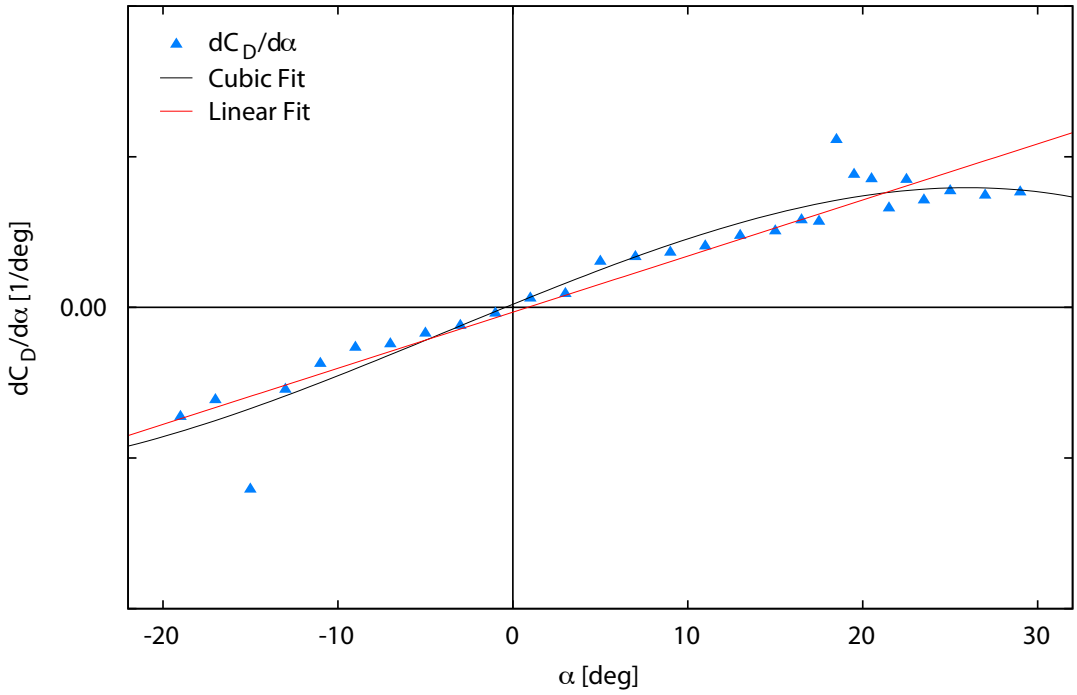

Figure 5.11: Fit result for $dC_D/d\alpha(\alpha)$

expansion to represent the change in C_D due to upflow. Figure 5.12 shows the effect of an upflow of $\Delta\alpha_{\text{up}} = 0.5°$ on $C_D(\beta)$. Data points represent measured data while solid lines show the value of C_D accounting for $\Delta\alpha_{\text{up}}$. At 0°, the interpolation produces virtually no discrepancy between the C_D curves. The rmse at 0° is 7.4×10^{-4}. The rmse increases linearly with increasing pitch angle, and reaches 1.4×10^{-2} at $\alpha = 14°$. Extrapolating, the drag uncertainty associated with the upflow correction could reach approximately 0.02 at $\alpha = 20°$.

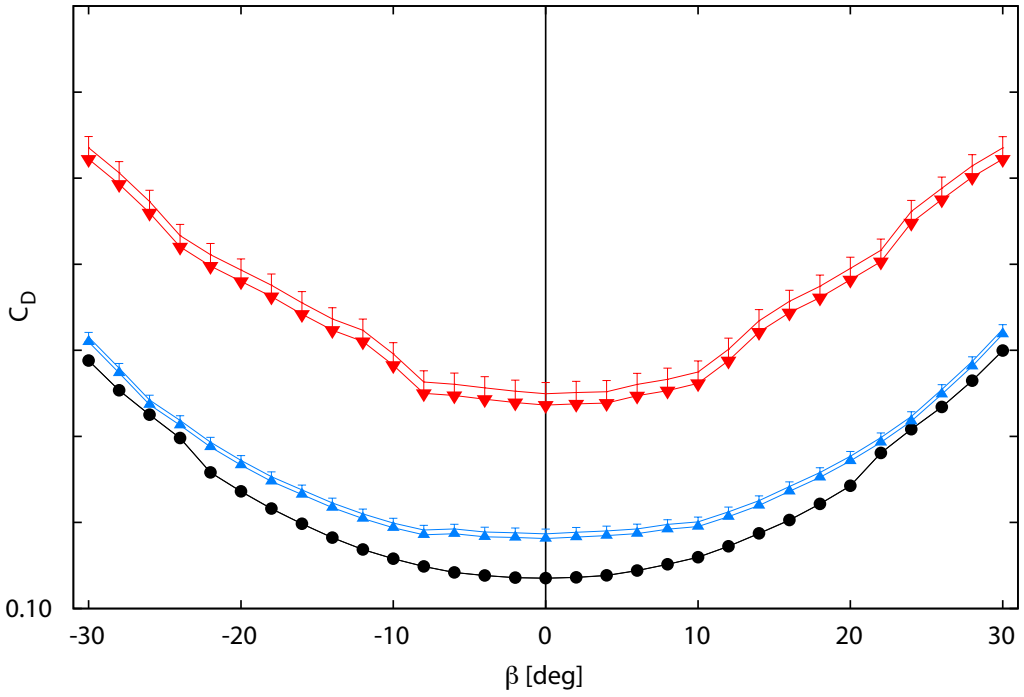

Figure 5.12: Effect of flow alignment on $C_D(\beta)$. Data points represent measured data, solid lines show aligned $C_D(\beta)$.

5.6 Moment Transfers to Model MRC

Forces and moments are then translated from wind-axis, balance-center (wabc) to wind-axis, model-center (wamc). In coefficient form, Equations 2.2 become

$$\begin{aligned} C_{\ell,\text{wamc}} &= C_{\ell,\text{wabc}} - \frac{y_{\text{MRC}}}{b} C_{Lu} - \frac{z_{\text{MRC}}}{b} C_{Yu} \\ C_{m,\text{wamc}} &= C_{m,\text{wabc}} - \frac{z_{\text{MRC}}}{c} C_{Du} + \frac{x_{\text{MRC}}}{c} C_{Lu} \\ C_{n,\text{wamc}} &= C_{n,\text{wabc}} + \frac{x_{\text{MRC}}}{b} C_{Yu} + \frac{y_{\text{MRC}}}{b} C_{Du} \end{aligned} \tag{5.8}$$

This operation applies only to measured moments, so no uncertainty is introduced into the force measurements. Additionally, b, c, and the position of the model MRC relative to the BMC $(x_{\text{MRC}}, y_{\text{MRC}}, z_{\text{MRC}})$ are considered exact because they are all reference dimensions. These dimensions do however effectively serve to amplify uncertainties of uncorrected force coefficients, resulting in an additional contribution to the uncertainty in the moment coefficients. Assuming no covariance between the external balance's force and moment readings,

$$\begin{aligned} \sigma^2_{C_{\ell,\text{wamc}}} &= \sigma^2_{C_{\ell,\text{wabc}}} + \left(\frac{y_{\text{MRC}}}{b}\right)^2 \sigma^2_{C_{Lu}} + \left(\frac{z_{\text{MRC}}}{b}\right)^2 \sigma^2_{C_{Yu}} \\ \sigma^2_{C_{m,\text{wamc}}} &= \sigma^2_{C_{m,\text{wabc}}} + \left(\frac{z_{\text{MRC}}}{c}\right)^2 \sigma^2_{C_{Du}} + \left(\frac{x_{\text{MRC}}}{c}\right)^2 \sigma^2_{C_{Lu}} \\ \sigma^2_{C_{n,\text{wamc}}} &= \sigma^2_{C_{n,\text{wabc}}} + \left(\frac{x_{\text{MRC}}}{b}\right)^2 \sigma^2_{C_{Yu}} + \left(\frac{y_{\text{MRC}}}{b}\right)^2 \sigma^2_{C_{Du}} \end{aligned} \tag{5.9}$$

5.7 Boundary Corrections

Recall that the wing is generating circulation to achieve lift. Furthermore, because a wing has tips (unlike an airfoil), spanwise flow moving from root to tip on the pressure side of the wing creates tip vortices which trail downstream. Due to the presence of the wind tunnel walls, the resulting flow pattern due to the wing's

circulation is altered. As discussed earlier, a horseshoe vortex is constructed with a bound vortex filament distributed along the wing's quarter-chord (with vorticity in the $+y_w$ direction) which turns 90° at the wingtips and continues downstream (with vorticity in the $\pm x_w$ direction).

For an infinite vortex filament, the induced vortical velocity at a distance r away is $v_\theta = -\Gamma/2\pi r$, where Γ is the circulation. The velocity w in the $-z_w$ direction is $w = v_\theta \cos\theta$ and the induced angle of attack along the centerline ($z = 0$) due to a single pair of image vortices located at $\pm h$ is:

$$\alpha_i(x) \approx w(x)/U_\infty = \left(\frac{c_L S}{2\pi}\right) \frac{x}{(x^2 + h^2)}$$

where c_L is the lift coefficient per unit span C_L/b. The approximation is further simplified by restricting the streamwise location of the correction to the wing quarter-chord on test section centerline. Figure 5.13 shows the flow field induced by a number of image vortex systems located at $\pm \mathrm{n} h, \mathrm{n} = 1 \ldots N$ relative to the test section centerline. The vertical velocity components are amplified for effect, showing the spatial variation of $\Delta\alpha_{\mathrm{sc}}$. Additionally, if the unstalled portion of the lift curve is approximated as a line:

$$C_L = 2\Gamma b/U_\infty S \approx a_0 \cdot \alpha$$

where a_0 is the lift-curve slope $dC_L/d\alpha$. This shows $\Gamma \propto \alpha$, which would cause further variation in $\Delta\alpha_{\mathrm{sc}}$.

The added wingtip vortex image systems cause a reduction in induced downwash, causing a wing to appear to have a larger aspect ratio than in reality. Figure 1.10 shows the general image setup for a pair of tip vortices located at $y_w = \pm b/2$. Again, since the total circulation must remain constant, the wing and its tip vortices are

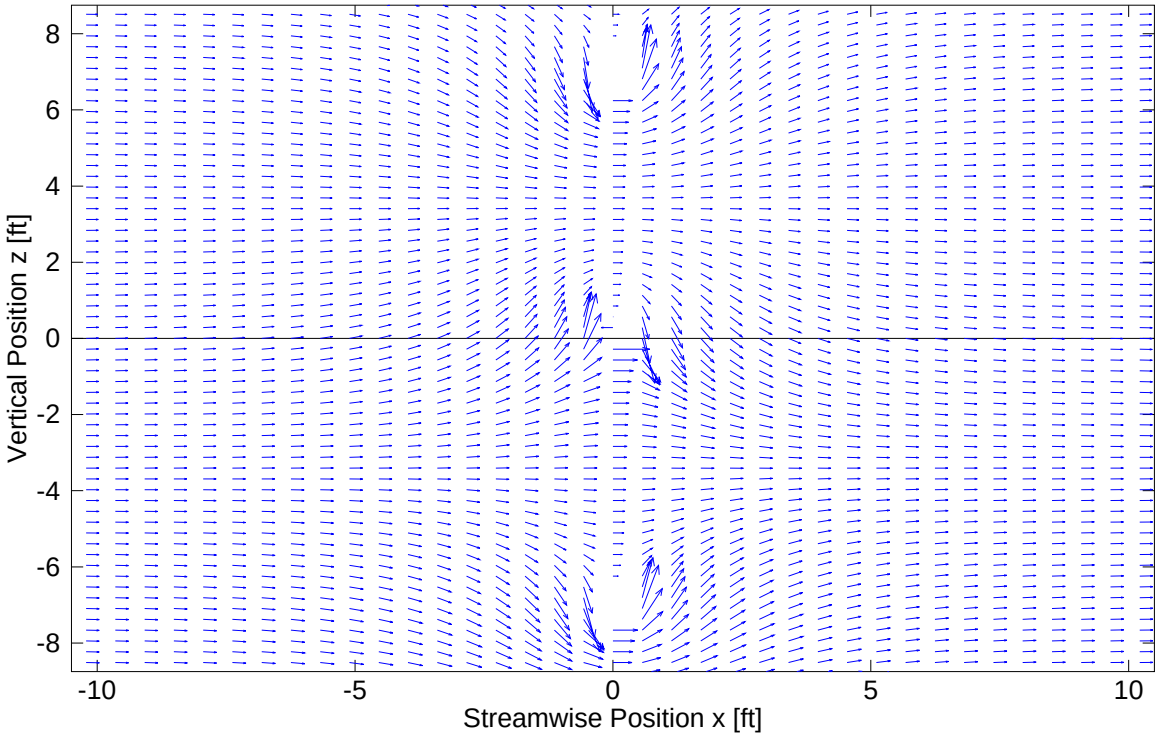

Figure 5.13: Induced flow field due to bound vortex and image systems

enclosed within a circular boundary of radius R. As before, the boundary becomes a streamline of the flow using the method of images (Figure 5.14). Because the tip vortices are of opposite sense relative to each other, so too must the image vortices. The induced downwash that would have been present in free flight is thus reduced, resulting in a decrease in both induced angle and in drag. Additionally, the tip vortices are modelled as semi-infinite vortex filaments because in two dimensions, they appear to originate at the wing's quarter-chord (unlike the spanwise vortex modelled as an infinite filament). Recall that the tip vortices are in fact part of a continuous horseshoe vortex so that Kelvin's circulation theorem is observed. It can be shown that the location of the image vortices must be at $\pm 2R^2/b$ in order to enforce the zero velocity condition at $r = R$. The vortical velocity induced by a semi-

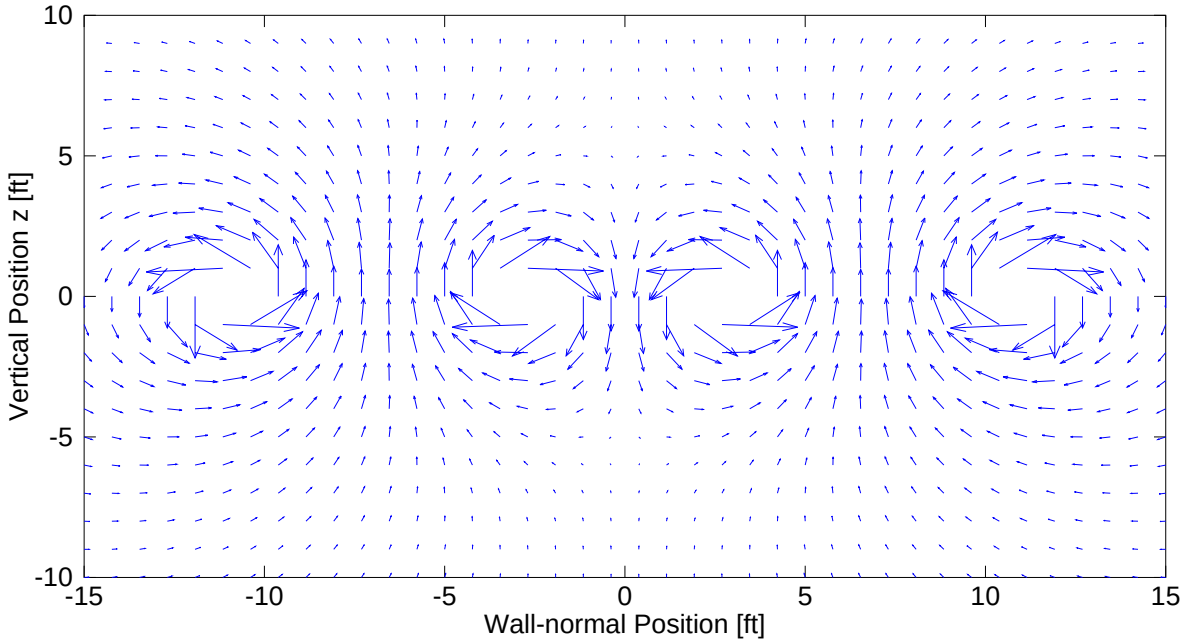

Figure 5.14: Induced flow field due to trailing vortices and image systems

infinite vortex filament at a distance r is $v_\theta = -\Gamma/4\pi r$, with horizontal and vertical components of $v_y = -v_\theta \sin\theta$ and $v_z = v_\theta \cos\theta$. Along the centerline, the induced vertical velocity due to the two image vortices at $(r, \theta) = (2R^2/b, 0)$ and $(2R^2/b, \pi)$ is

$$v_z = 2\frac{\Gamma}{4\pi}\frac{b}{2R^2} = \frac{SU_\infty}{8\pi R^2}C_L$$

Noting that for this case, the test section cross-sectional area $C = \pi R^2$, the change in induced upflow due to normal downwash is

$$\Delta\alpha_i \approx \frac{v_z}{U_\infty} = \frac{1}{8}\left(\frac{S}{C}\right)C_L = \delta\left(\frac{S}{C}\right)C_L$$

For the circular test section represented in Figure 1.10 with wing on centerline, $\delta = 0.125$ is exact. Changes to δ arise from different test section cross-sectional profiles and from differing test setups.

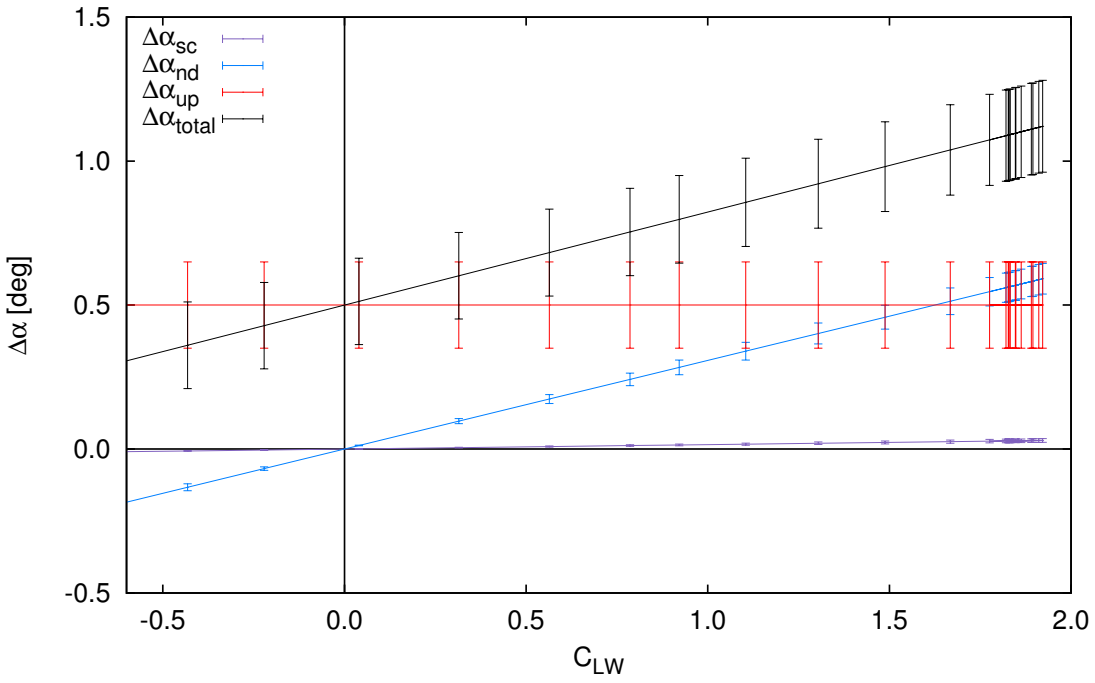

Figure 5.15: Magnitudes of induced angles of attack due to upflow, streamline curvature, and normal downwash

In order to define uncertainties for the boundary corrections, the empirical data for correction factors are compared with the theoretical results. Based on the figures given in Barlow et al., $\sigma_\delta = 0.01$, $\sigma_{\tau_{2,\text{wing}}} = 0.01$ and $\sigma_{\tau_{2,\text{tail}}} = 0.1$.

Figures 5.15 and 5.16 show the induced angle of attack as a function of C_{LW}. Figure 5.15 shows induced angle magnitudes, while Figure 5.16 shows the contribution of each correction to the total angularity correction. From both figures, it is evident that the induced angle of attack due to streamline curvature is negligible as its the magnitude is bounded by the uncertainty in $\Delta\alpha_{\text{up}}$. This flow angularity causes a change in lift due to the altered flow field which results in induced drag.

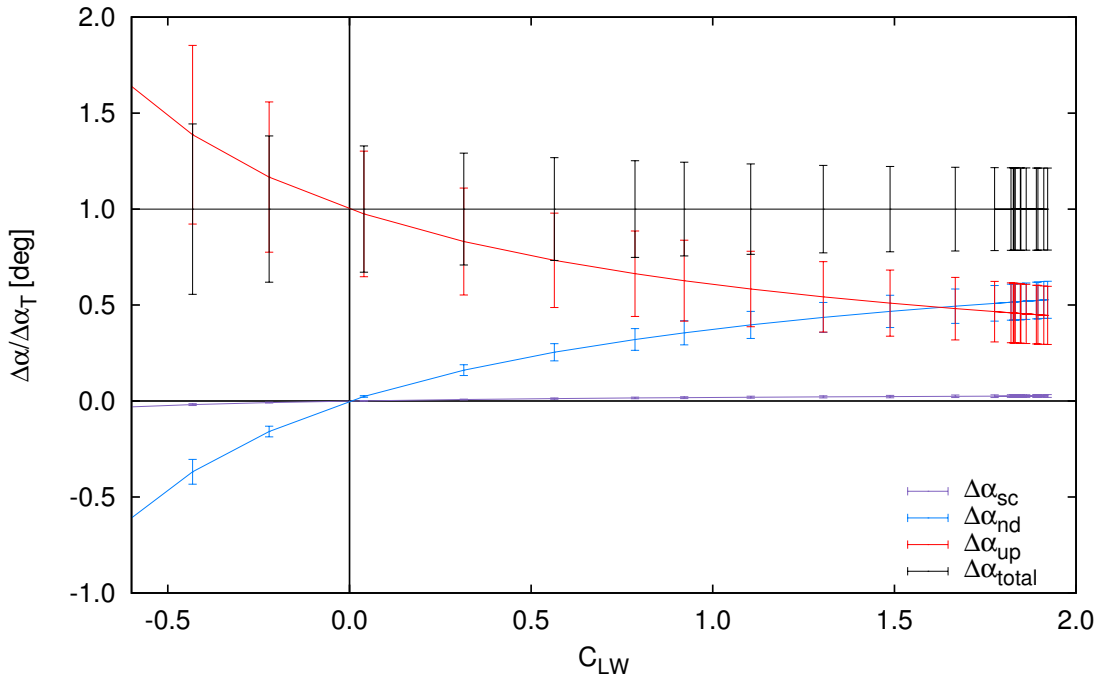

Figure 5.16: Contributions of induced angles of attack to total angularity correction

From the boundary correction discussion above,

$$C_{Dc} = C_{Du} + \underbrace{C_{LW}\Delta\alpha_{\text{up}}}_{\Delta C_{D,\text{up}}} + \underbrace{\delta\frac{S}{C}C_{LW}^2}_{\Delta C_{D,\text{nd}}}$$

This is an appropriate approximation due to the magnitude of the two induced angles. Currently, the streamline curvature correction does induce any drag force, nor do the downwash or upflow corrections induce lift force. From Barlow et al., $C_{D,\text{aligned}} = C_{D,\text{meas}} + C_{L,\text{meas}} \tan\Delta\alpha_{\text{up}} \approx C_{D,\text{meas}} + C_{L,\text{meas}}\Delta\alpha_{\text{up}}$. The latter term in the preceding equation is the same as $\Delta C_{D,\text{up}}$ from Equation 3.15, so one must be careful to apply the correction only once.

The standard approach does not correct $C_{L,\text{meas}}$ for misalignment. If the lift-to-

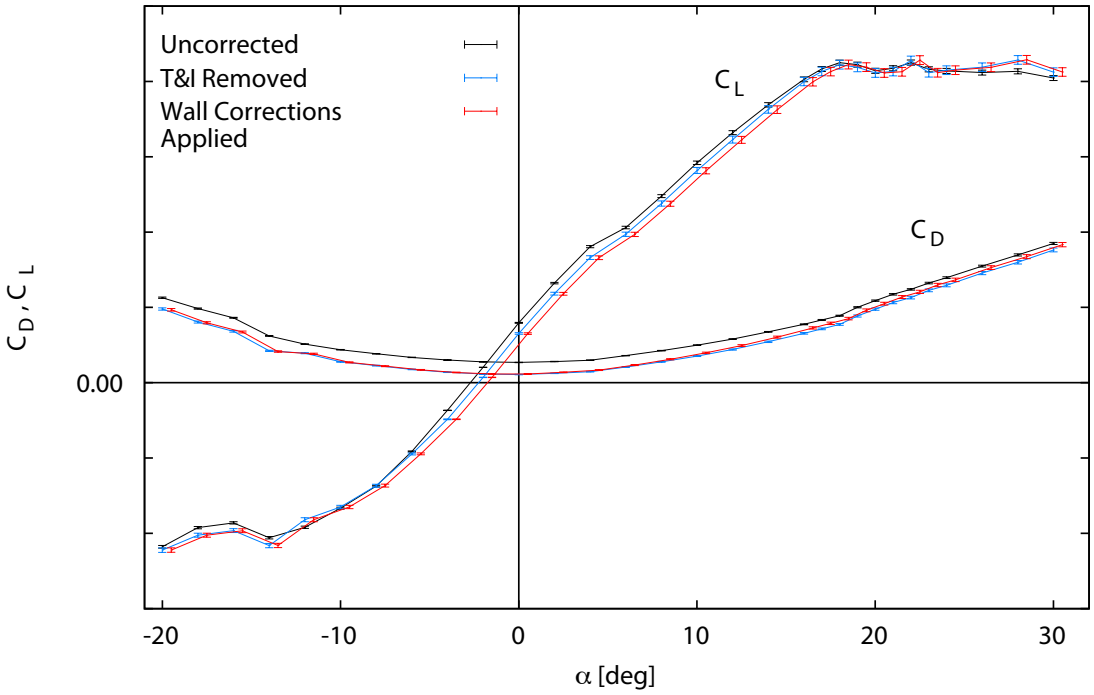

Figure 5.17: Effect of data reduction process on lift and drag force

drag ratio L/D is assumed large for aerodynamic vehicles, the induced lift due to drag is less consequential than the converse. From a theoretical standpoint, it may be incorrect to include the induced angle due to streamline curvature in the expression for α_c given in standard practice (Section 3) because the streamline curvature effect does not impart a constant upward flow angularity to the entire flow field (see Fig. 5.13). Similarly, the angle induced by the trailing tip vortices affects the flow aft of the wing's quarter-chord location. A change in angle of attack may accurately represent the change in vehicle response but does not affect the angularity of the global flow field. Figures 5.17 and 5.18 show the effect of the data reduction process for pitching moment and the lift and drag force. Note the increased uncertainty in the wall-corrected C_D as C_L passes through stall.

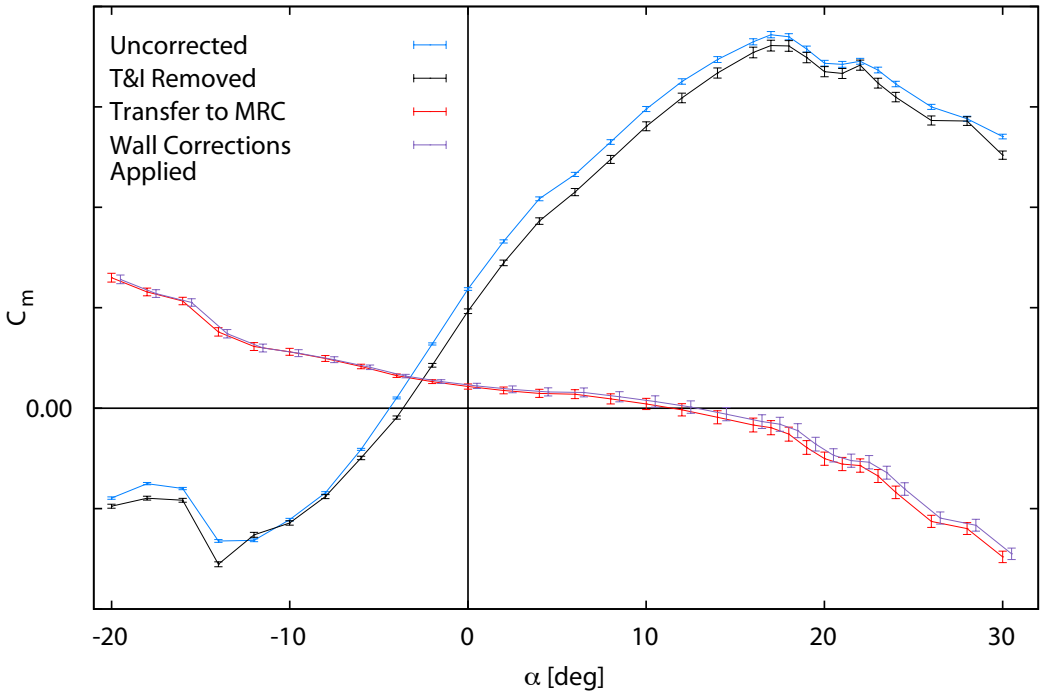

Figure 5.18: Effect of data reduction process on pitching moment

6. SUMMARY AND RECOMMENDATIONS

The goal of this thesis is to characterize the uncertainty associated with the standard data analysis procedure used for wind tunnel testing. While the majority of the procedure does not require approximation, the final step in the process relies heavily on it. As discussed earlier a facility with near-perfect precision can produce repeatable data, which is an important step in evaluating the aerodynamic stability of the vehicle. The precise data may not be accurate however, i.e., it may still not be representative of the behavior of the vehicle in flight. The application of boundary corrections is the current solution to this problem. The model for doing so may be outdated however.

Throughout the preceding arguments, the uncertainty associated with each step of the process was quantified. Doing this allowed an assessment of each component's overall contribution to the error present in the final data. The static tare mathematical model and fitting process proved to be a precise method for computing, verifying and predicting wind-off moments. Additionally, the static tare methodology has a sufficiently small uncertainty. As such, it should be used in future wind tunnel testing to improve operational efficiency without loss of precision.

The remaining steps introduce additional uncertainty into the finalized data. The point-by-point T&I subtraction method is acceptable, but would produce a more accurate result if inverted data is first interpolated to eliminate the $\Delta\alpha_{\text{up}}$ discrepancy between inverted and upright configurations. The upflow angle should be calculated using the shooting method approach as it yields the lowest uncertainty with the best estimate of upflow. Because the upflow angle is an artifact of the experimental setup and test section, it should be treated as a change in reference frame prior to

performing the other boundary corrections. Doing so will still account for the drag contamination resulting from upflow. The streamline curvature correction borders on trivial because the magnitude of $\Delta\alpha_{\text{sc}}$ is negligible compared to the other angularity corrections. This causes insignificant changes to the lift force and pitching moment. The streamline curvature correction should still be applied, however, because the goal is to obtain representative free-flight data. Furthermore, $\Delta\alpha_{\text{sc}}$ should not be included in the correction to angle of attack due to its variability, though the error introduced by doing so is small. The flow angularity due to the normal downwash correction contributes much more to the overall correction to angle of attack. Finally, the alignment correction should be applied to both the lift and drag forces. The most accurate application of this correction would be to treat the correction as a reference frame change. This requires use of the rigorous equations including the trigonometric terms rather than making small angle approximations so that:

$$C_{D,\text{aligned}} = C_{D,\text{meas}} \cos\Delta\alpha_{\text{up}} + C_{L,\text{meas}} \sin\Delta\alpha_{\text{up}}$$
$$C_{L,\text{aligned}} = -C_{D,\text{meas}} \sin\Delta\alpha_{\text{up}} + C_{L,\text{meas}} \cos\Delta\alpha_{\text{up}}$$

The small-angle approximations lead to an approximate discrepancy of 6×10^{-5}, so it is at the discretion of the test engineer to apply the correction as necessary.

In conclusion, the standard approach leads to a maximum aerodynamic force coefficient uncertainty of 0.1 and a maximum moment coefficient uncertainty of 0.04. The recommended modifications to this approach do not reduce the overall uncertainty, but produce a more accurate result from a theoretical standpoint. These claims can be readily verified by comparing wind tunnel test data to full scale flight vehicle diagnostics. Due to the nature of the atmosphere however, any readings taken in free-flight are subject to even greater measurement uncertainties due to freestream

fluctuations, foreign object strikes, etc. As such, it may not be possible to obtain a true metric of the accuracy of wind tunnel data relative to free-flight data.

REFERENCES

[1] Baals, D. D. and Corliss, W. R., *Wind Tunnels of NASA*, Scientific and Technical Information Branch, National Aeronautics and Space Administration, 1981.

[2] Barlow, J. B., Rae Jr., W. H., and Pope, A., *Low-Speed Wind Tunnel Testing*, Wiley & Sons, Unites States of America, 1999.

[3] Glauert, H., *Wind Tunnel Interference on Wings, Bodies and Airscrews*, H.M. Stationery Office, London, 1933.

[4] Anderson Jr., J. D., *Fundamentals of Aerodynamics*, McGraw-Hill Companies, Unites States of America, 2007.

[5] Hidore, J. P., *Investigation of Data Quality For Wind Tunnel Internal Balance Testing*, Master's thesis, Texas A&M University, 2013.

[6] Bevington, P. and Robinson, D. K., *Data Reduction and Error Analysis for the Physical Sciences*, McGraw-Hill Companies, Unites States of America, 1992.

APPENDIX A

TEST SETUP AND LSWT FACILITY FIGURES

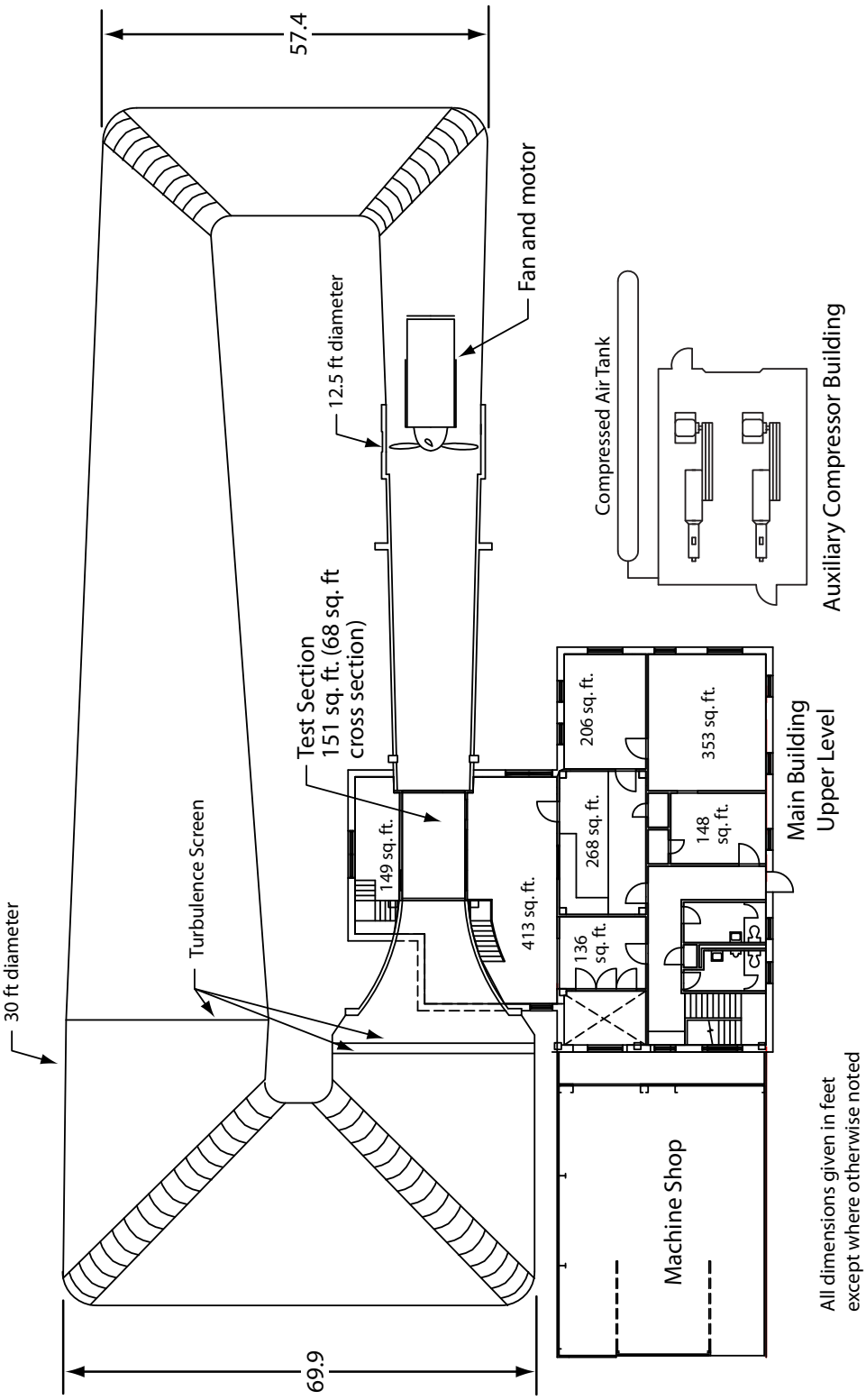

Figure A.1: Schematic view of the LSWT.

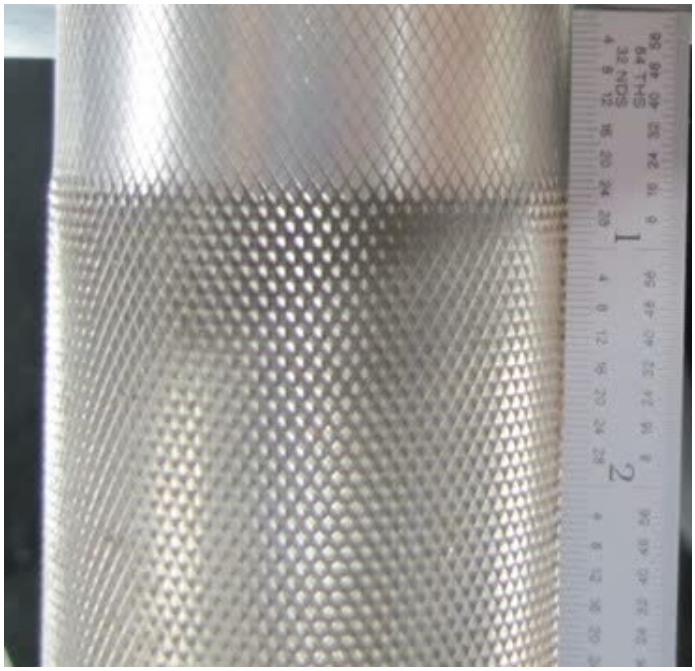

Figure A.2: Knurling on main strut

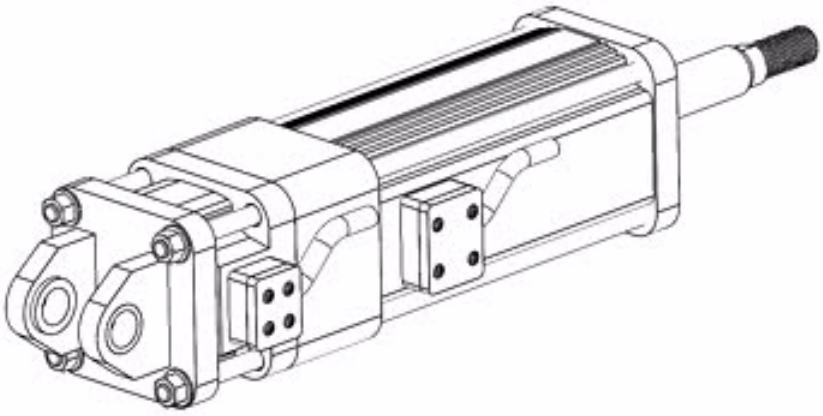

Figure A.3: GSX40 linear actuator

APPENDIX B

REFERENCE TABLES

$K_1 = 1.095$	
$\tau_{1,\mathrm{w}} = 0.865$	$B/H = 1.4286$, $2b/B = 0.476$
$K_{3,\mathrm{b}} = 0.932$	
$\tau_{1,\mathrm{b}} = 0.865$	$B/H = 1.4286$, $2b/B = 0$

Table B.1: Solid blockage constants

$\delta = 0.1125$	$b_e/B = 0.476$, $H/B = 0.7$
$\tau_{2,\mathrm{wing}} = 0.05$	$l_t/B = 0.017$
$\tau_{2,\mathrm{tail}} = 0.6$	$l_t/B = 0.233$

Table B.2: Streamline curvature constants

σ	**Description**	**Maximum Value**
F	Force Measurement Uncertainty	0.2% of applied load
M	Moment Measurement Uncertainty	0.2% of applied load
α_g	Geometric Angle of Attack	0.1°
ψ	Yaw Angle	0.1°
ϵ_{sb}	Incremental Solid Blockage Velocity	$\epsilon_{\mathrm{sb}} \approx 4 \times 10^{-3}$
q_{act}	Uncorrected Dynamic Pressure	0.2 psf
M_T	Moment Gravity Tare	1 ft·lb$_f$
$\Delta\alpha_{\mathrm{up}}$	Upflow Angle	0.15°
$C_{F,\mathrm{wabc}}$	T&I-removed Force Coefficient	0.02
$C_{M,\mathrm{wabc}}$	T&I-removed Moment Coefficient	0.03
δ	Boundary Correction Factor	0.01
τ_{2w}	Wing Downwash Correction Factor	0.01
τ_{2t}	Tail Downwash Correction Factor	0.1
$C_{F,\mathrm{corrected}}$	Fully Corrected Force Coefficient	0.030
$C_{M,\mathrm{corrected}}$	Fully Corrected Moment Coefficient	0.035

Table B.3: Data reduction uncertainties